Master's thesis

NTNU
Norwegian University of Science and Technology
Faculty of Natural Sciences
Department of Physics

Solveig Uv Sundlisæter

Adsorption of CO and CO_2 on mica surfaces doped with 3*d* transition metal oxides

A DFT investigation

Master's thesis in Applied Physics and Mathematics
Supervisor: Jon Andreas Støvneng
December 2018

NTNU
Norwegian University of
Science and Technology

Solveig Uv Sundlisæter

Adsorption of CO and CO_2 on mica surfaces doped with 3*d* transition metal oxides

A DFT investigation

Master's thesis in Applied Physics and Mathematics
Supervisor: Jon Andreas Støvneng
December 2018

Norwegian University of Science and Technology
Faculty of Natural Sciences
Department of Physics

NTNU
Norwegian University of
Science and Technology

Abstract

The adsorption of carbon dioxide (CO_2) and carbon monoxide (CO) on mica surfaces doped with metal oxides has been studied, with the intention of finding suitable materials for carbon storage. The metals tested are the $3d$ transition metals Mn, Fe, Co, Ni, Cu and Zn. The computational tool density functional theory (DFT) in the Kohn-Sham approach is used to find stable adsorption sites and calculate adsorption energies and activation barriers. Additionally, analyses of charge transfer and density of states are performed. The employed exchange-correlation functional is the revised Perdew-Burke-Ernzerhof (revPBE) functional within the generalised gradient approximation (GGA).

CO_2 adsorption results in the formation of a negatively charged carbonate group on all the surfaces. MnO-mica seems to be the most promising surface for CO_2 adsorption, with the largest adsorption energy E_{ads} = 2.11 eV and no energy barrier. Energy barriers for chemisorption are detected on the surfaces with Fe, Co, Ni and Cu, and the barriers are generally smaller on the surfaces with more stable chemisorption structures.

CO adsorption gives two chemisorption sites for all surfaces, where the most energetically favourable site gives a bent, negatively charged CO_2 moiety. The surface that has the strongest interaction with CO is NiO-mica, with the adsorption energy E_{ads} = 2.53 eV. The alternative geometry involves CO bonding to the metal through the carbon atom. Even though this geometry is less stable, the bonding is relatively strong for most of the surfaces with adsorption energies in the range 0.28 - 1.36 eV.

Sammendrag

Adsorpsjon av karbondioksid (CO_2) og karbonmonoksid (CO) på micaoverflater dopet med metalloksider har blitt studert med den hensikt å finne egnede materialer for karbonlagring. Metallene som ble testet er $3d$-overgangsmetallene Mn, Fe, Co, Ni, Cu og Zn. Modelleringsverktøyet tetthetsfunksjonalteori (DFT) med Kohn-Sham tilnærming er brukt for å finne stabile geometrier og regne ut bindingsenergier og aktiveringsbarrierer. I tillegg har analyser av ladningsoverføring og tilstandstetthet blitt utført. Utvekslings-korrelasjons funksjonalet revidert Perdew-Burke-Ernzerhof (revPBE) i den generaliserte gradient approksimasjonen (GGA) er tatt i bruk.

CO_2-adsorpsjon resulterer i formasjonen av en negativt ladet karbonat-gruppe på alle overflatene. MnO-mica ser ut til å være den mest lovende overflaten for CO_2-adsorpsjon, med den høyeste bindingsenergien $E_{\text{ads}} = 2.11$ eV og ingen energibarriere. Energibarrierer for adsorpsjon er funnet for overflatene med Fe, Co, Ni og Cu, og barrierene er generelt lavere for overflater med mer stabile kjemisorberte strukturer.

CO-adsorpsjon gir to kjemisorberte strukturer for alle overflatene, der den mest energisk gunstige strukturen gir en bøyd, negativt ladet CO_2-gruppe. Overflaten som har den sterkeste bindingen til CO er NiO-mica, med en bindingsenergi på $E_{\text{ads}} = 2.53$ eV. Den alternative geometrien innebærer CO-binding til metall-atomet gjennom karbon-atomet. Selv om denne geometrien er mindre stabil, er bindingen relativt sterk for de fleste overflatene med bindingsenergier i området 0.28 - 1.36 eV.

Preface

This thesis was written as a conclusion of the five year master program in Applied physics and mathematics at the Norwegian University of Science and Technology (NTNU). It is a continuation of my specialisation project, which was written in the spring of 2018. The work for this thesis was carried out during the autumn of 2018.

I would first and foremost like to thank my supervisor Jon Andreas Støvneng, who has given me a lot of his time and provided excellent guidance and feedback. Additionally, I am grateful for the support team at the computational chemistry software company SCM, which have given quick and thorough responses to my questions and been truly helpful.

Lastly, I would like to thank my friends and family. Especially, my parents and my boyfriend Pre, whose support and encouragement has been invaluable.

Table of Contents

Abbreviations

CO_2 = Carbon dioxide
CO = Carbon monoxide
DFT = Density Functional Theory
XC = Exchange-Correlation
KS = Kohn-Sham
SCF = Self-Consistent Field
LDA = Local Density Approximation
GGA = Generalised Gradient Approximation
PW91 = Perdew-Wang 1991 functional
PBE = Perdew-Burke-Ernzerhof
revPBE = revised Perdew-Burke-Ernzerhof
GTO = Gaussian Type Orbitals
STO = Slater Type Orbitals
PES = Potential Energy Surface
TS = Transition State
AMS = Amsterdam Modelling Suite
SCM = Software for Chemistry & Materials
NAO = Numerical Atomic Orbitals
DOS = Density of States

1 | Introduction

1.1 Motivation and background

The vast majority of scientists agree that climate change is happening and that the most important cause is the increasing use of fossil fuels since the industrial revolution. In 2009, the world's governments agreed on the goal to keep warming under 2°C above the pre-industrial temperatures. The latest report from The Intergovernmental Panel on Climate Change (IPCC) from 2014 stated that to achieve this goal, the emission of greenhouse gases must be reduced by 40 - 70% from 2010 to 2050 [1]. Simultaneously, the world population is growing and so is the energy demand. Some of the increasing demand can be met by emission-free energy sources, but it is not sufficient [2]. Technology for capturing and storing greenhouse gases like carbon dioxide (CO_2) has therefore been researched and used, but these methods need an upgrade towards more efficient, cheap and safe methods. The adsorption of carbon monoxide (CO) is also interesting to study with energy storage and carbon capture in mind.

Previous studies have shown that clay materials are able to adsorb CO_2 and therefore might be suitable for carbon capture [3, 4]. In 1989, Bhattacharyya managed to adsorb CO_2 on a vacuum cleaved and hydrogen atom bombarded air-cleaved muscovite mica surface [5]. Mica, which is a type of clay, is therefore an interesting material to study further. In my specialisation project, a pure mica and a nickel-mica surface were considered, and their abilities to adsorb CO and CO_2 were compared using the computational method Density Functional Theory (DFT) [6]. As the nickel-mica surface adsorbed both molecules considerably better than the pure mica surface, different surfaces of metals on mica are worth investigating.

CO_2 is known to adsorb on various metal oxides. For example, on $TiO_2(110)$ CO_2 bonds weakly to regular fivefold coordinated Ti^{4+} atoms [7]. CO_2 adsorption on a mix-terminated $ZnO(10\bar{1}0)$ surface has been studied with some different conclusions for the adsorption geometry. One study where DFT, He-atom scattering (HAS) and high-resolution electron energy loss spectroscopy (HREELS) were all employed, found that a negatively charged carbonate ion with a tridentate configuration was formed. The two oxygen atoms in CO_2 bonded with two surface zinc atoms, and the carbon atom bonded to a surface oxygen atom [8]. Due to the positive effect metal oxides seem to have, different surfaces will here be created by placing a layer of a metal oxide on top of mica and compare the surfaces' affinities towards CO_2 and CO. The metals that are studied are the 3*d* transition metals Mn, Fe, Co, Ni, Cu and Zn, which are chosen to check whether any interesting trends may be observed.

As in my specialisation project, the computational method DFT will be used for the calculations. DFT is a quantum mechanical modelling tool used to do theoretical studies of the electronic structure of a many-body problem using numerical methods and making some necessary approximations [9].

1.2 The structure of muscovite mica

Muscovite mica is the most common mica material, and can be found naturally in various rock types [5]. It is a periodic bulk crystal, and its structure is therefore described by the repeating unit, called the *unit cell*, which is the basic input into a DFT calculation. When repeated in all three directions, the unit cell produces the entire 3-dimensional structure [10].

Mica belongs to the monoclinic crystal system. The unit cell of a monoclinic crystal has the form depicted in figure 1.1, with lattice vectors forming a rectangular prism [11]. Two of the angles formed by the lattice vectors are 90°, while the last angle, β is 95.18°. The length of the lattice vectors are a_1 = 5.189 Å, a_2 = 8.995 Å and a_3 = 20.097 Å [12].

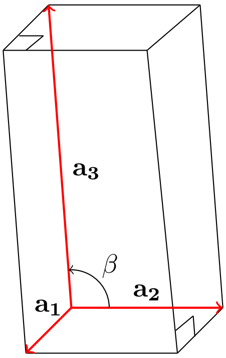

Figure 1.1: The shape of the unit cell of a monoclinic crystal system. The lattice vectors $\mathbf{a_1}$, $\mathbf{a_2}$ and $\mathbf{a_3}$ are marked with red arrows.

Muscovite mica is a layered aluminosilicate with the chemical formula $KAl_2(Si_3Al)O_{10}(OH)_2$ [13]. Figure 1.2 shows the [100] projection of mica, with the unit cell repeated twice side by side. Each irreducible layer consists of three layers; two tetrahedral silicate layers where one fourth of the Si^{4+} ions is replaced with an Al^{3+} ion, and, between these, a layer with octahedrally coordinated Al^{3+} ions. Due to the trivalent aluminium being substituted for the tetravalent silicon, these three layers have a net negative charge [5]. To compensate for that, positive potassium K^+ ions are positioned on both sides of the three-layered structure. Because of the weak bonds between the potassium ions and the aluminosilicate layers, the material is easy to cleave along its layers [13]. There are 84 atoms in the unit cell.

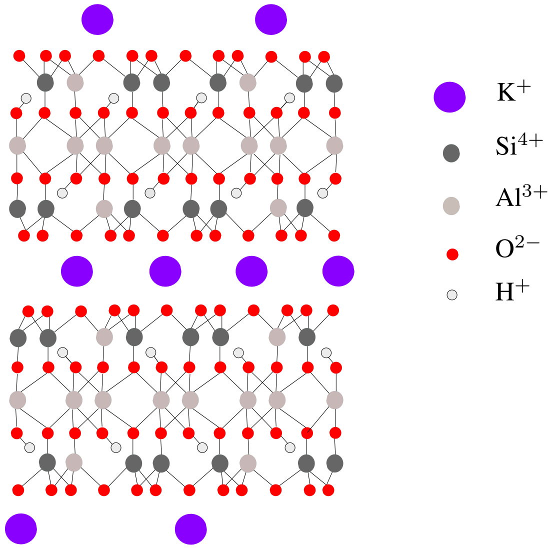

Figure 1.2: The structure of muscovite mica, in the [100] projection. The colour code for the atoms is continued throughout the report.

1.3 Structure of the report

In chapter 2, the theory behind the DFT calculations is explained. The computational details with the specifications used in the calculations are stated in chapter 3. In chapter 4, the results and discussion of the results are presented, and chapter 5 includes the conclusion and thoughts on further work within the topic.

As the work behind the report is a continuation of my specialisation project [6], most of the theory section from the project is still relevant here. Therefore, sections 1.2, 3.2, 3.3 and parts of Chapter 2 are based on reference [6].

2 | Theoretical background for DFT

In this chapter the problem of solving the many-body Schrödinger equation will be presented, together with two different approaches to solving the problem computationally. The main focus will be on DFT and some aspects related to it, as DFT is the method used for the calculations. I will first, however, briefly present the Hartree-Fock method, which is interesting to consider in relation to DFT and is based on many of the same ideas. The main reference for the chapter is [9].

2.1 A many-body problem

The Schrödinger equation is a fundamental quantum mechanical equation that describes the behaviour of a many-body physical system [14]. It is useful for calculating the electronic arrangement and energies of a system. To define the position of an atom, both the position of the nucleus and all its electrons must be defined, which makes the task quite complicated in cases with many atoms. An effective approximation to simplify the problem is based on the fact that the nucleus is significantly heavier than one electron, so the electrons respond faster to change than the nucleus. The nuclei may therefore be fixed in the calculation while the electrons are free to move around, and the electron equations are solved. This approach is known as *the Born-Oppenheimer approximation* [15]. The electron configuration with the lowest energy, the so-called *ground state*, can then be found. The ground state energy is expressed as a function of the nuclei positions, $E(\mathbf{R}_1, ..., \mathbf{R}_M)$.

The electrons are described by the electron wave function $\psi = \psi(\mathbf{r}_1, ..., \mathbf{r}_N)$, where $\mathbf{r}_i$ is the position of electron i. Evidently, the wave function is a function of the 3 spatial coordinates of all the N electrons. It is a solution to the many-electron time-independent Schrödinger equation,

$$\hat{H}\psi = \left[-\frac{\hbar^2}{2m} \sum_{i=1}^{N} \nabla_i^2 + \sum_{i=1}^{N} V(\mathbf{r}_i) + \sum_{i=1}^{N} \sum_{j<i} U(\mathbf{r}_i, \mathbf{r}_j) \right] \psi = E\psi, \tag{2.1}$$

where $\hat{H}$ is the energy operator, called the *Hamiltonian*, E is the total energy of the electrons and m is the electron mass. The first term describes the kinetic energy of each electron, $V(\mathbf{r}_i)$ is the potential arising from the interaction between the electron at $\mathbf{r}_i$ and the collection of nuclei, and $U(\mathbf{r}_i, \mathbf{r}_j)$ the interaction potential between the electron at $\mathbf{r}_i$ and another at $\mathbf{r}_j$. As the problem has $3N$ variables, it will become untractable quite fast as the number of electrons in the system increases. It seems useful to split the wave function into a number of wave functions for each individual electron, as these will only depend on 3 variables, namely the spatial coordinates for one electron. Unfortunately, the electron-electron interaction term makes it impossible to get an exact solution with the individual electron wave functions. One individual wave function cannot be found without considering the wave functions for all the other electrons, which makes it a many-body problem.

2.2 The Hartree-Fock method

One way to overcome the complexity of solving the Schrödinger equation is to neglect interaction between the electrons. Then the total Hamiltonian for the system can be approximated as

$$H = \sum_{i=1}^{N} h_i, \tag{2.2}$$

where h_i is the Hamiltonian of electron i. The single-electron Schrödinger equation is $h\chi$ = $E\chi$, with χ as spin orbital eigenfunctions. For each electron, there are multiple spin orbitals, so χ defines the set $\chi_j(\mathbf{x}_i)$ (j =1,2,...). The vector $\mathbf{x}_i$ defines the position and spin state of electron i. The energy of spin orbital χ_j is E_j. The wave functions for the N-electron system, which are the eigenfunctions of H, can be written as products of the single-electron spin orbitals χ as [16]

$$\psi(\mathbf{x}_1, ..., \mathbf{x}_N) = \chi_{j1}(\mathbf{x}_1)\chi_{j2}(\mathbf{x}_2)...\chi_{jN}(\mathbf{x}_N). \tag{2.3}$$

This is called the *Hartree product.* The energy corresponding to the total wave function is the sum of the spin orbital energies E_j.

To model the physical world in the most accurate way, the electron wave functions should reflect the properties of the electrons. Electrons are fermions and obey the *Pauli exclusion principle*, which states that only one fermion can occupy the same quantum state simultaneously [17]. They also obey the antisymmetry principle, which is a consequence of the Pauli exclusion principle, and states that an exchange of two electrons will change the sign of the wave function. This is not true in general for the Hartree product, which is a major drawback. The shortcoming gave way to the Hartree-Fock method [18], where the Slater determinant is used as an expression for the wave function for the total N-electron-system. The Slater determinant for an N-electron-system is [19]

$$\psi(\mathbf{x}_1, ..., \mathbf{x}_N) = \frac{1}{\sqrt{N!}} \begin{vmatrix} \chi_1(\mathbf{x}_1) & \chi_2(\mathbf{x}_1) & \cdots & \chi_N(\mathbf{x}_1) \\ \chi_1(\mathbf{x}_2) & \chi_2(\mathbf{x}_2) & \cdots & \chi_N(\mathbf{x}_2) \\ \vdots & \vdots & \ddots & \vdots \\ \chi_1(\mathbf{x}_N) & \chi_2(\mathbf{x}_N) & \cdots & \chi_N(\mathbf{x}_N) \end{vmatrix}.$$

For the special case with only two electrons, the wave function becomes

$$\psi(\mathbf{x}_1, \mathbf{x}_2) = \frac{1}{\sqrt{2}} \left[\chi_1(\mathbf{x}_1)\chi_2(\mathbf{x}_2) - \chi_1(\mathbf{x}_2)\chi_2(\mathbf{x}_1) \right]. \tag{2.4}$$

It is apparent that if the two electrons are put in the same spin orbital, equivalent to χ_1 = χ_2, the wave function $\psi(\mathbf{x}_1, \mathbf{x}_2)$ becomes zero. Hence, the Pauli exclusion principle is satisfied. The wave function will also change sign upon the exchange of two electrons, thereby obeying the antisymmetry principle. Additionally, it does not distinguish between the electrons, which is another important property in quantum mechanics.

The Slater determinant provides a way to split the total Schrödinger equation (2.1) into many single-electron equations

$$\left[-\frac{\hbar^2}{2m}\nabla^2 + V(\mathbf{r}) + V_H(\mathbf{r}) \right] \chi_j(\mathbf{x}) = E_j \chi_j(\mathbf{x}). \tag{2.5}$$

The first two terms have the same interpretation as those in equation (2.1), while the interaction term is here replaced by the *Hartree potential* $V_H(\mathbf{r})$,

$$V_H(\mathbf{r}) = e^2 \int \frac{n(\mathbf{r}')}{|\mathbf{r} - \mathbf{r}'|} d^3 r'. \tag{2.6}$$

The potential represents the Coulomb repulsion between the electron considered and the total electron density of all the other electrons.

Due to the antisymmetric nature of the Slater determinant, exchange interaction is included in the method. However, correlation effects are neglected to some extent, and the Coulomb repulsion is included only in an average way through the Hartree potential [20].

The spin orbital wave functions are continuous functions, and must therefore be redefined using a finite amount of information to be described computationally. A solution is to approximate them using a finite set of K basis functions, $\phi_1(\mathbf{x}), \phi_2(\mathbf{x}), ..., \phi_K(\mathbf{x})$, called the *basis set*. The result is

$$\chi_j(\mathbf{x}) = \sum_{i=1}^{K} \alpha_{j,i} \phi_i(\mathbf{x}). \tag{2.7}$$

Here, $\alpha_{j,i}$ are the expansion coefficients, with i = 1,...,K and j = 1,...,N. The size of the basis set will affect the accuracy of the calculation, and a larger basis set leads to higher computational cost. Choosing good basis functions, that are similar to the real spin orbitals also improves the accuracy.

The quantities necessary to solve the Schrödinger equation with the Hartree-Fock method are now defined. However, due to the circular nature of the method, the calculation must be done iteratively. First, an initial guess for the spin orbitals is made, which is used to calculate the electron density $n(\mathbf{r}')$. Then the single-electron equations (2.5) are solved to find the spin orbitals. If these are similar enough to the initial guess for the spin orbitals, we have reached the correct solution. If not, the guess for the spin orbitals is updated and the calculations are repeated.

Because the correlation of the electrons are not taken into account, the Hartree-Fock method often leads to results with large deviations from experiment. It is therefore time to consider DFT, a method which includes both exchange and correlation energies.

2.3 DFT and the electron density

DFT is another computational method used to find solutions to the Schrödinger equation. Although the origins of the theory are considered to be the papers by Hohenberg and Kohn [21] from 1964 and Kohn and Sham [22] from 1965, it did not become a widespread tool for modelling materials until the 1990s [23]. Since then the application of DFT has grown remarkably, and today it is a standard method that is used regularly by researchers in several areas within material science.

As opposed to the Hartree-Fock method, DFT is an electron density-based method, rather than a wave-function based method. The electron density $n(\mathbf{r})$, giving the density of electrons at position $\mathbf{r}$, is used to map a many-body problem into a single-body problem. It is an important quantity in DFT as it reduces the number of dimensions of the problem from $3N$ to 3, which makes a big difference for larger systems. The idea of using the electron density for determining the electronic structure of many-body problems originated from Thomas and Fermi and their so-called Thomas-Fermi model from the 1920s [24, 25].

The electron density can be expressed as

$$n(\mathbf{r}) = 2\sum_i \psi_i^*(\mathbf{r})\psi_i(\mathbf{r}). \tag{2.8}$$

Here, $\psi_i(\mathbf{r})$ is the individual electron wave function, and $\psi_i^*(\mathbf{r})\psi_i(\mathbf{r})$ gives the probability that an electron with wave function $\psi_i(\mathbf{r})$ is positioned at $\mathbf{r}$. The Pauli exclusion principle states that two electrons can only occupy the same state if they have different spins, hence the factor 2 in front of the summation. The electron density only depends on 3 variables, but still contains a large part of the information the Schrödinger equation gives.

Two theorems presented by Hohenberg and Kohn in 1964 became essential for DFT [21]:

1. *The ground state energy is a unique functional of the electron density.*

2. *The electron density that minimises the energy of the functional is the correct electron density that corresponds to the solution of the Schrödinger equation.*

A functional is a quantity that takes in a function and returns a single number. The first theorem expresses that the relation given in equation (2.8) can be reversed, which means that for a given ground state electron density, the corresponding ground state wave function and energy can be uniquely determined. The ground state energy is then written as $E\left[n(\mathbf{r})\right]$. To find the ground state electron density we use the second theorem, which suggests that the variational principle can be used to find the ground state electron density. The variational principle involves starting with an approximate electron density, and varying it until the energy is minimised.

The energy functional in terms of the single-electron wave functions $\psi_i(\mathbf{r})$ can be written as

$$
\begin{aligned}
E\left[\{\psi_i\}\right] = &-\frac{\hbar^2}{2m}\sum_i \int \psi_i^* \nabla^2 \psi_i d^3r + \int V(\mathbf{r}) n(\mathbf{r}) d^3r \\
&+ \frac{e^2}{2}\int\int \frac{n(\mathbf{r})n(\mathbf{r}')}{|\mathbf{r}-\mathbf{r}'|} d^3r d^3r' + E_{ion} + E_{XC}\left[n\right].
\end{aligned}
\tag{2.9}
$$

The first term represents the kinetic energy of the electrons, the second the Coulomb interaction between the electrons and the nuclei, the third the Coulomb interaction between pairs of electrons, and the fourth the Coulomb interaction between pairs of nuclei. Finally, $E_{XC}\left[n\right]$ is the exchange-correlation functional, which incorporates the quantum mechanical effects not included in the other terms. Its exact form is not yet known, but we assume that there is an approximate way to express it, which we will get back to in section 2.5. After overcoming this obstacle, what remains to solve the problem and find the electron density is a set of single-electron equations. These were presented by Kohn and Sham in 1965.

2.4 The Kohn-Sham equations

In 1965, Kohn and Sham introduced what is now known as the Kohn-Sham equations, a set of equations describing the motion of individual electrons [22]. The many-body problem is split into many single-body problems, making the problem simpler to solve. The correlation between the electrons is still included through the approximated exchange-correlation functional, which is the most difficult part remaining in solving the problem. The equations can be expressed as

$$
\left[-\frac{\hbar^2}{2m}\nabla^2 + V_{eff}(\mathbf{r})\right]\psi_i(\mathbf{r}) = \epsilon_i \psi_i(\mathbf{r}),
\tag{2.10}
$$

where $V_{eff}(\mathbf{r})$ = $V(\mathbf{r})$ + $V_H(\mathbf{r})$ + $V_{XC}(\mathbf{r})$ is the effective potential in which the electrons move. The first term here is the same that appears in the second term of the Schrödinger equation in (2.1), and defines the interaction between the individual electrons and the collection of nuclei. The second term is the Hartree potential, as defined in equation (2.6). It includes the unphysical interaction of the electron with itself, which is one of several effects that is corrected for by the third term, the exchange-correlation potential $V_{XC}(\mathbf{r})$. It covers the exchange and correlation contributions to the electron, and is defined as the functional derivative of the exchange-correlation energy

$$
V_{XC} = \frac{\delta E_{XC}\left[n\right]}{\delta n(\mathbf{r})}.
\tag{2.11}
$$

In order to solve the Kohn-Sham equations, we need to know the electron density $n(\mathbf{r})$ as it appears in the Hartree potential. To calculate the electron density, we need the wave functions $\psi_i(\mathbf{r})$, which again are found by solving the Kohn-Sham equations. Due to the circular nature of the problem, the best solution is to treat it iteratively, similar to the Hartree-Fock method. This is done as follows:

1. An initial electron density $n(\mathbf{r})$ is defined.
2. The Kohn-Sham equations (2.10) are solved using the defined electron density from point 1, and the wave functions $\psi_i(\mathbf{r})$ are found.
3. A new electron density, $n_{KS}(\mathbf{r})$ is calculated from equation (2.8) using the wave functions found in step 2.
4. If the two electron densities $n(\mathbf{r})$ and $n_{KS}(\mathbf{r})$ are similar enough, we say that convergence is reached, and the correct ground state electron density is found. If not, the initial electron density is updated, and the iterative process is repeated from point 2 until the energy is converged towards a self-consistent solution. The convergence criterion is chosen by the user and determines how similar the solutions have to be before they are converged. It is chosen based on the level of accuracy needed and what is affordable in terms of computer time. The convergence procedure is termed self-consistent field (SCF) convergence.

The resulting converged electron density is used to calculate the total energy.

2.5 The exchange-correlation functional

There is still something missing to solve the Kohn-Sham equations, namely an expression for the exchange-correlation functional, $E_{XC}\left[n\right]$. The problem is that the exact form of the functional is not known for a system with an arbitrary electron density $n(\mathbf{r})$, so an approximate expression must be used. There are several ways to do the approximation, two of which are called the *local density approximation* (LDA) and the *generalised gradient approximation* (GGA).

2.5.1 LDA - The local density approximation

The LDA formulation is based on the uniform electron gas, a simple system where the electron density is constant in terms of the position in space. At each position $\mathbf{r}$, the exchange-correlation energy for each infinitesimal element $n(\mathbf{r})d\mathbf{r}$ is set to be equal to the exchange-correlation energy known in a uniform electron gas with the electron density $n(\mathbf{r})$ [22],

$$E_{XC}^{LDA}\left[n\right] = \int n(\mathbf{r})\varepsilon_{XC}^{LDA}(n(\mathbf{r}))d\mathbf{r}. \tag{2.12}$$

Here, $\varepsilon_{XC}\left[n\right]$ is the exchange-correlation energy per electron of a uniform electron gas, which consists of an exchange term $\varepsilon_X\left[n\right]$ and a correlation term $\varepsilon_C\left[n\right]$. The exchange term is based on calculations for the homogeneous electron gas, and was found to be [20]

$$\varepsilon_X^{LDA}(n) = -\frac{3}{4}\frac{3}{\pi}^{1/3} n^{1/3}(\mathbf{r}). \tag{2.13}$$

The contribution from the correlation term $\varepsilon_C\left[n\right]$ comes from Coulomb interaction between the electrons. A parametrisation of the correlation energy can be obtained from a quantum Monte Carlo simulation of a uniform electron gas at varying electron densities [20].

Even though the electron density is not uniform in real materials, and the LDA functional seems extremely simplified, it has had great success and produces fairly accurate results. However, LDA functionals tend to overestimate atomisation energies, so a more accurate approach is needed.

2.5.2 GGA - The generalised gradient approximation

The class of functionals that is defined from the *generalised gradient approximation* is an improved version of the LDA, as it includes the electron density gradient as well as the electron density. A variety of functionals implementing the idea exist, where the difference between them is how the gradient is included in the functional. The different implementations of the GGA functionals result in varying performances, and they are not necessarily more accurate than the LDA functionals. However, they tend to improve the total energy and atomisation energy calculations compared to LDA, especially for more non-uniform materials. The functionals PW91 (Perdew-Wang 1991) [26], PBE (Perdew-Burke-Ernzerhof) [27] and revPBE (revised PBE) [28] are examples of functionals that employ the GGA approach.

In general, the GGA exchange-correlation functional is given by [27]

$$E_{XC}^{GGA}[n] = \int f(n(\mathbf{r}), \nabla n(\mathbf{r}))d\mathbf{r}, \tag{2.14}$$

where f is some function of $n(\mathbf{r})$ and $\nabla n(\mathbf{r})$. The functional is divided into an exchange part, E_X^{GGA} and a correlation part, E_C^{GGA}. The correlation term takes various forms depending on the functional, while the exchange term is generally given by

$$E_X^{GGA}[n] = \int n\varepsilon_X^{LDA}(n)F_X(s)d\mathbf{r}. \tag{2.15}$$

Here, $\varepsilon_X^{LDA}(n)$ is the uniform exchange energy as used in LDA and $F_X(s)$ is an enhancement factor for local exchange [29]. The argument s is the reduced dimensionless density gradient, defined as

$$s(\mathbf{r}) = \frac{\mid \nabla n(\mathbf{r}) \mid}{2(3\pi^2)^{1/3}n(\mathbf{r})^{4/3}}. \tag{2.16}$$

For a uniform gas, $s = 0$ as $\nabla n(\mathbf{r}) = 0$, and the criterion $F_X(0) = 1$ must hold to obtain the correct result [27].

The difference between the exchange functionals lie in the quantity $F_X(s)$. For PW91, $F_X(s)$ is [26]

$$F_X(s) = \frac{1 + 0.19645s\sinh^{-1}(7.7956s) + (0.2743 - 0.1508e^{-100s^2})s^2}{1 + 0.19645s\sinh^{-1}(7.7956s) + 0.004s^4}. \tag{2.17}$$

PBE was developed to be similar to PW91, but with simpler expressions and fewer parameters. The enhancement factor for PBE is

$$F_X^{PBE}(s) = 1 + \kappa - \frac{\kappa}{1 + \mu s^2/\kappa^2}, \tag{2.18}$$

where the constants are κ = 0.804 and μ = 0.235. The revPBE functional is identical to PBE, but revised so that κ = 1.245. The small alteration has shown to give improved atomic total energies and atomisation energies of molecules [28].

2.5.3 Dispersion correction

A problem with all GGA functionals is that they do not model van der Waals forces, which may be relevant in long-range electron correlations. They are especially important for weakly bonded systems. For many years research has been conducted to find a way to model the dispersion interactions and incorporate them into the energy functional. One suggestion was made by Grimme in 2006 [30], his method termed DFT-D, which was later revised into DFT-D3 in 2010 [31]. Both methods involve adding a dispersion correction term to the Kohn-Sham energy, giving a total energy of

$$E_{DFT-D(3)} = E_{KS-DFT} + E_{disp}. \tag{2.19}$$

E_{KS-DFT} is the original Kohn-Sham energy and E_{disp} is an empirical dispersion correction, given by [31]

$$E_{disp} = \sum_{AB} \sum_{n=6,8,10,...} s_n \frac{C_n^{AB}}{r_{AB}^n} f_{d,n}(r_{AB}). \tag{2.20}$$

AB denotes an atom pair, C_n^{AB} is the n-th order averaged dispersion coefficient for atom pair AB and r_{AB} is the distance between the atoms A and B. s_n are global scaling factors, and $f_{d,n}$ is the damping function used to determine the range of the dispersion correction.

In DFT-D, the dispersion coefficients are derived empirically, while in the improved version they are calculated from first principles using time-dependent DFT. They are atom pairwise specific and geometry dependent. Tests have shown that the improved method performs far better for heavier systems especially [31].

2.6 Reciprocal space and Bloch's theorem

The material investigated here is a periodic bulk crystal, and is, as mentioned in section 1.2, described by the unit cell, the repeating part of the periodic arrangement. In real space, the position of each unit cell is defined by

$$\mathbf{R} = n_1\mathbf{a_1} + n_2\mathbf{a_2} + n_3\mathbf{a_3}. \tag{2.21}$$

Here, n_1, n_2 and n_3 are arbitrary integers, and $\mathbf{a_1}$, $\mathbf{a_2}$ and $\mathbf{a_3}$ are the lattice vectors. These define the crystal axes, which form the edges of the unit cell [10].

It is relevant to look at the concept of reciprocal space, as large parts of the calculations in a DFT problem are easier to solve here than in real space. In reciprocal space, the $\mathbf{k}$-vectors are the equivalent to the $\mathbf{r}$-vectors in real space. The *Brillouin zone*, which is the unit cell of the reciprocal space, is defined by the lattice vectors $\mathbf{b_1}$, $\mathbf{b_2}$ and $\mathbf{b_3}$. These are related to the real space lattice vectors $\mathbf{a_1}$, $\mathbf{a_2}$ and $\mathbf{a_3}$ by [10]

$$\mathbf{b_1} = 2\pi \frac{\mathbf{a_2} \times \mathbf{a_3}}{\mathbf{a_1} \cdot (\mathbf{a_2} \times \mathbf{a_3})}, \quad \mathbf{b_2} = 2\pi \frac{\mathbf{a_3} \times \mathbf{a_1}}{\mathbf{a_2} \cdot (\mathbf{a_3} \times \mathbf{a_1})}, \quad \mathbf{b_3} = 2\pi \frac{\mathbf{a_1} \times \mathbf{a_2}}{\mathbf{a_3} \cdot (\mathbf{a_1} \times \mathbf{a_2})}. \tag{2.22}$$

The vectors are defined such that $\mathbf{a_i} \cdot \mathbf{b_j}$ = 2π for i = j and 0 otherwise. If we choose a to be the length of the lattice vector, $|\mathbf{a_i}|$ = a, then $|\mathbf{b_i}|$ = $2\pi/a$. Consequently, a large unit cell gives a small Brillouin zone.

Bloch's theorem states that the solution of the Schrödinger equation for a periodic system can be expressed as [32]

$$\Phi_{\mathbf{k}}(\mathbf{r}) = e^{i\mathbf{k}\cdot\mathbf{r}} u_{\mathbf{k}}(\mathbf{r}). \tag{2.23}$$

Here, $u_{\mathbf{k}}(\mathbf{r})$ is a function that has the same periodicity as the unit cell, i. e. $u_{\mathbf{k}}(\mathbf{r} + n_1\mathbf{a_1} + n_2\mathbf{a_2} + n_3\mathbf{a_3})$ = $u_{\mathbf{k}}(\mathbf{r})$. Wave vectors differing by any reciprocal lattice vector $\mathbf{G}$ therefore give the same wave function, where

$$\mathbf{G} = m_1\mathbf{b_1} + m_2\mathbf{b_2} + m_3\mathbf{b_3}. \tag{2.24}$$

Thus, by exploiting the periodicity, all useful information can be found in the first Brillouin zone, and we will not need infinitely many wave functions even though the material is infinite. The Brillouin zone has several high-symmetry points that are especially interesting, the most important one being the point where $\mathbf{k}$ = 0, called the Γ-point.

2.7 K-space sampling

In a DFT calculation, integrals are evaluated over all possible k-values in the Brillouin zone. A computer has to do the integration discretely, which is done by substituting the integration with a summation. This approximation is possible because the wave functions change slowly as $\mathbf{k}$ is varied. An appropriate k-point sampling must be chosen. Naturally, the more k-points used, the more accurate the result is, but the computational time also increases substantially. In 1976, Monkhorst and Pack developed a method for generating special points in the Brillouin zone to efficiently integrate periodic functions [33]. The sampling k-points are distributed homogeneously throughout the Brillouin zone. The number of k-points to use in each direction of the lattice must be specified, which put together becomes $M_1 \times M_2 \times M_3$ for a three-dimensional material. The density of k-points should be equal in all directions, which means that for $|\mathbf{b_1}| > |\mathbf{b_2}|$, M_1 should be larger than M_2.

To check that the results are sufficiently accurate, a convergence test with respect to the number of k-points is conducted. A number of calculations are performed with varying number of k-points, for example measuring the total energy of the system. When the total energy is almost independent of the number of k-points, the results are said to be well converged.

2.8 Basis sets and the frozen core approximation

The periodic function $u_{\mathbf{k}}(\mathbf{r})$ from Bloch's theorem mentioned earlier, is expanded in a set of basis functions. The basis can be composed of plane waves, or atomic orbitals. Gaussian Type Orbitals (GTOs) and Slater Type Orbitals (STOs) are examples of atomic orbitals that can be used. The most common one in DFT calculations is GTOs, but for the program used here, STOs are employed. The form of the approximate functions is

$$\psi = R_{nl}(r)Y_{lm}(\theta, \phi). \tag{2.25}$$

$Y_{lm}(\theta, \phi)$ are the spherical harmonics, and for Slater-type orbitals, the radial part $R_{nl}(r)$ is [34]

$$R_{nl}(r) = (2\zeta)^{n+1/2}\left[(2n)!\right]^{-1/2} r^{n-1} e^{-\zeta r}. \tag{2.26}$$

Here, n is the principal quantum number, l the angular momentum quantum number and ζ is related to the effective charge of the nucleus. This expression has a similar form to the solution of the Schrödinger equation for hydrogen-like atoms, and its exponential decay is a desirable quality as the orbitals of DFT decay in the same way.

Basis sets come in varying sizes, where the largest offer a higher accuracy, but at a higher computational cost. The smallest basis set is the *minimal basis set*, also called *single zeta*, which only contains one function for each orbital in the atom [35]. The accuracy using the single zeta basis set is normally insufficient for research use. The next level is the *double zeta* basis, for which the number of functions used is doubled compared to the single zeta. Further, the larger basis sets are called *triple zeta*, *quadruple zeta*, etc.

The basis functions used are centred on the atomic nuclei. This leads to an error as the atom in a molecule will not have the same charge distribution as in an isolated atom, but rather be perturbed because the electrons are attracted to the nuclei of the other atoms. A solution to the problem is to add polarisation functions to the basis set.

Wave functions of the core electrons do not affect the bonds the atom forms, and they are virtually unaffected by changes in the surroundings. Therefore, a reasonable approximation is to fix the innermost electrons during the SCF procedure to decrease the calculation time. The number of electrons to fix are chosen depending on the affordability in terms of calculation time and the level of accuracy needed. The approximation is termed the *frozen core approximaton*.

2.9 Potential energy surface

The *potential energy surface* (PES) of a system is a plot of the potential energy as a function of all the coordinates involved. A nonlinear molecule with N atoms has $3N$-6 independent coordinates [36]. A simplified, one dimensional curve can be created by only considering one chosen coordinate. The stationary points, which is where the gradient vanishes, may then be classified based on the curvature of the potential energy surface at each point. The curvature is the second derivative of the energy with respect to every coordinate, whose components make up the so-called *Hessian matrix* $\mathbf{H}$,

$$\mathbf{H} = \begin{bmatrix} \frac{\partial^2 E}{\partial x_1^2} & \frac{\partial^2 E}{\partial x_1 \partial y_1} & \cdots & \frac{\partial^2 E}{\partial x_1 \partial z_A} \\ \vdots & & \ddots & \vdots \\ \frac{\partial^2 E}{\partial z_A \partial x_1} & \frac{\partial^2 E}{\partial z_A \partial y_1} & \cdots & \frac{\partial^2 E}{\partial z_A^2} \end{bmatrix}.$$

A is the number of atoms in the system. The stationary points where the Hessian matrix has only positive eigenvalues, are energy minima, which correspond to physically stable states. As the system moves from one minimum to another, it could take a number of paths, but the most interesting one is the minimum energy path, i.e. the path with the smallest change in energy. It will always pass through a point termed the *transition state* (TS), which is a maximum on the reaction pathway, but a minimum in all other directions. The Hessian therefore has exactly one negative eigenvalue at the transition state; it is a first order saddle point [35].

The eigenvectors of the Hessian are the vectors $\mathbf{e}$ that satisfy $\mathbf{He} = \lambda \mathbf{e}$, where λ are the eigenvalues. There are $3A$ eigenvalues λ_i which give the vibrational frequencies of motion ν_i for the system through the relation [9]

$$\nu_i = \frac{1}{2\pi}\sqrt{\frac{\lambda_i}{m}}. \tag{2.27}$$

The frequencies represent the normal modes of vibration. A linear combination of the normal modes gives the most general movement of the system. The type of vibration giving rise to each frequency can be read from the corresponding eigenvector, which states the magnitude of the fluctuation by each atom in every direction.

Equation (2.27) shows that the negative eigenvalue at the transition state corresponds to an imaginary frequency. All the other frequencies should be either zero or real. One of the $3N$-6 vibrational degrees of freedom corresponds to movement along the reaction path, and the remaining ones represent vibration orthogonal to it [36].

The energy required for the system to overcome the energy barrier from one minimum to another, say from **B** to **A**, is termed the *activation energy* of the reaction, and is defined by [9]

$$E_{\mathrm{a}} = E(\mathbf{TS}) - E(\mathbf{B}). \tag{2.28}$$

Here $E(\mathbf{TS})$ is the energy at the transition state and $E(\mathbf{B})$ is the energy at minimum **B**. It is useful to compare the activation energy with typical thermal energies. According to statistical mechanics, for a system in equilibrium the average energy available to each degree of freedom is $k_BT/2$, where k_B is Boltzmann's constant. The thermal energy is 0.013 eV at room temperature. Even if the activation energy is larger than this, there is at every point in time a certain probability that the system will gain enough energy to overcome the barrier, due to collisions and interactions between the atoms. The rate of the reaction from **B** to **A**, defined by the number of reactions per second $k_{\mathbf{B}\to\mathbf{A}}$, is given by the Arrhenius equation [37]

$$k_{\mathbf{B}\to\mathbf{A}} = Ae^{-E_{\mathrm{a}}/k_BT}. \tag{2.29}$$

Here, A is the pre-exponential factor, or frequency of collisions in the correct direction. The factor e^{-E_a/k_BT} gives the probability that one collision will result in a reaction.

Adsorption processes with a significant activation energy are said to be *activated*. This is the case for certain cases of *chemisorption*, which are adsorptions where a chemical reaction takes place between the surface and the adsorbate. These processes typically involve breaking of bonds and formation of new ones, and must therefore overcome an energy barrier to occur. Other characterisations of chemisorption are short bond distances, large adsorption energies and charge transfer between the adsorbate and the surface [38].

Physisorption is an adsorption reaction with weaker bonding, longer bond lengths and no activation barrier. The forces involved are mostly weak van der Waals forces. There is no definite value of adsorption energy that separates chemisorbed from physisorbed systems, but one indication of chemisorption can be that the adsorbate is altered relative to the free gas version.

To illustrate the concept of potential energy surfaces, an example of CO_2 adsorbed on nickel in a periodic arrangement is included. The one dimensional potential energy surface with respect to the carbon-nickel bond is plotted in figure 2.1.

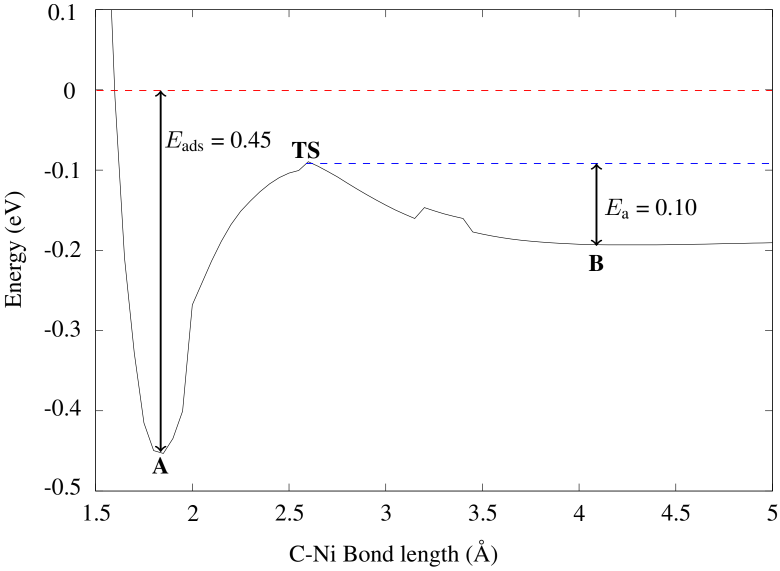

Figure 2.1: The potential energy surface with respect to the C-Ni bond length for CO_2 adsorbed on nickel. The zero energy level is defined as the sum of the energy of the free CO_2 molecule and the nickel surface.

The plot shows two local energy minima, **A** and **B**. Minimum **A** represents a geometry where the CO_2 molecule is perturbed from the free molecule with an O-C-O angle of 180° to 152.7° in the adsorbed geometry. The carbon-nickel bond length is 1.85 Å, which is relatively short. Both these facts suggest that the CO_2 molecule is chemisorbed in this geometry. In minimum **B**, the CO_2 molecule is virtually not altered from the free molecule form, the carbon-nickel bond length is 4-5 Å and the adsorption energy is 0.19 eV. The adsorption here is therefore of a physisorbed character. There is clearly an energy barrier that must be overcome to get from **B** to **A**, on which the transition state (**TS**) is the highest point. The height of the barrier is the activation energy E_a = 0.10 eV. This is about 8 times the thermal energy at room temperature, and gives a probability for reaction of 4.6×10^{-4} for one collision at room temperature. Combined with the collision frequency, which is assumed to be of similar or higher magnitude, the probability is more than high enough to get an activated reaction.

3 | Computational details

The calculations in this thesis were performed using DFT, as implemented by the Amsterdam Modelling Suite (AMS) program. AMS has been developed and operated by the Software for Chemistry & Materials (SCM) since 1995. As the system of interest is periodic, the BAND package, employing periodic DFT code, was used [39]. BAND uses STOs together with Numerical Atomic Orbitals (NAOs) as basis sets [40].

3.1 Geometry optimisation

The bulk mica structure was first pre-optimised as stated in reference [6]. The mica surface was prepared by removing the bottom half of the bulk structure, leaving behind 42 atoms in the unit cell, and then geometry optimising using the "slab" option within BAND. Further, the surfaces were geometry optimised with and without the adsorbate to calculate adsorption energies. These geometry optimisations were performed with the two bottoms layers, containing 11 atoms, fixed. The lattice vectors of the mica surface are a_1 = 5.56 Å and a_2 = 9.64 Å, found from a series of calculations optimising the lattice, as stated in reference [6]. The employed settings for the geometry optimisations are stated in the following.

The exchange-correlation potential chosen was the revised Perdew-Burke-Ernzerhof (revPBE) functional from the generalised gradient approximation, which results in a higher accuracy than the local gradient approximation with only marginally higher computational cost. The employed basis set was the *double zeta*, with one polarisation function (DPZ). The next level basis set *triple zeta* with one polarisation function (TZP) was found to be too time consuming for the mica system. The frozen core approximation has the options None - Small - Medium - Large, which reflects the number of atomic orbitals being fixed. Here, the option "Large" was chosen to speed up the calculation.

The "Numerical quality" key has the options Basic - Normal - Good - Very good - Excellent, and influences the quality of several aspects of the calculations; the Becke grid, Zlm Fit, k-space integration and Soft Confinement. The Becke grid is a numerical integration grid developed by Becke [41]. Zlm Fit is the splitting of the total electron density into atomic densities, which are approximated by radial spline functions and spherical harmonics (Zlm). The k-space integration quality chosen determines the number of k-points used in each direction depending on the size and shape of the unit cell. For a k-space integration set to "Good", the total number of unique k-points is 13, and for "Normal" it is

5. The numerical quality for these calculations was set to "Normal", which means that all the above aspects are set to "Normal".

The geometry optimisations are run to find a self-consistent energy minimum, and are said to be converged when the convergence criteria are met. Here the default values of the convergence criteria were used, which are: 0.001 Hartree for the energy change from the current geometry to the geometry of the previous iteration, 0.001 Hartree/Angstrom for the nuclear gradients, 0.01 Angstrom for changes in bond length and 0.5 degrees for changes in bond- and dihedral angles.

3.2 Mulliken population analysis

The density of states (DOS) was calculated for the stable structures. To find the partial density of states, *Mulliken population analysis* was used [42]. This is an orbital based method for estimating atomic partial charges. The atomic orbitals are expanded in basis functions, which make up a definition of the total density matrix. To partition the electrons between the atoms, the charge belonging to the basis functions of each atom is assigned to that atom [43].

A "Small" frozen core was applied for these calculations to involve a larger number of orbitals.

3.3 Bader charge analysis

A *Bader charge analysis* was run on the most stable adsorption systems, to calculate the charge transfer between the adsorbate and the surface. It is a different method for decomposing the charge density into contributions from each of the atoms in the system, which is based on *the quantum theory of atoms and molecules*, as proposed by Bader in 1990 [44]. This theory defines some important chemical concepts which are all derived from the electron density. The idea behind the method is to divide space into regions, whose boundaries are at a minimum in charge density, which is typically the boundaries between atoms in a molecule. The surfaces partitioning the regions should then satisfy the zero-flux condition, namely that the gradient of the charge density is zero along the surface normal, $\nabla n(\mathbf{r}) \cdot \hat{n} = 0$.

The algorithm used by ADF is grid-based, meaning that an integration grid in real space is partitioned into regions, which each represents one atom. The zero-flux surfaces are not found explicitly. Instead, the space is partitioned into small cubes which center around each point in the grid, and the ascending gradient path that passes through each point of the grid is followed until a point of maximum density is reached. Based on this, each cube is associated to a region. To find the charge density of each atom, an integration is done over all the grid points in the region [45].

The Bader analysis is performed on the fitted density. Therefore, to get more exact results for the charges, the Zlm fit quality was set to "Very Good" for these calculations. Additionally, a "Small" frozen core was applied. For the other options, the same settings were applied as for the geometry optimisations.

3.4 Linear transit calculations

To find the magnitude of the activation energies for the adsorption processes, their potential energy curves were found by running a PES scan for each process. It was, however, necessary to simplify the graph by only considering one coordinate, namely the distance from the adsorbate to the surface. The special one dimensional case is called a *linear transit*. The adsorbate is first placed far away from the surface, and the structure is geometry optimised with the distance fixed and allowing all other variables to relax. The distance is then changed to be slightly smaller, and a new geometry optimisation is performed still with the distance fixed. The process is continued for as many steps as are chosen along the interval. The curve then shows how the energy changes as the adsorbate gets closer to the surface. All the linear transit calculations were performed employing the same settings as for the geometry optimisations.

4 | Results and discussion

4.1 Comparing functionals

To get an idea of how the exchange-correlation functional employed affects the result of a DFT calculation, the functionals PW91, PBE and revPBE were compared. The converged geometries from the specialisation project, which were obtained using PW91, were geometry optimised again with the functionals PBE and revPBE. The effect of adding a dispersion correction to the functional was also investigated, by adding the dispersion correction D3 to revPBE. The resulting adsorption energies of CO and CO_2 to mica and nickel-mica are presented in table 4.1. All the adsorption energies E_{ads} were calculated using

$$E_{\text{ads}} = E(\text{surface}) + E(\text{adsorbate}) - E(\text{adsorbate/surface}), \tag{4.1}$$

where $E(\text{surface})$ is the energy of the surface, $E(\text{adsorbate})$ is the energy of the free adsorbate molecule and $E(\text{adsorbate/surface})$ is the energy of the converged adsorption geometry.

Table 4.1: The adsorption energies E_{ads} of CO and CO_2 to mica and nickel-mica using the functionals PW91, PBE, revPBE and revPBE-D3, where the latter includes a dispersion correction. The unit is eV. The results for PW91 are from reference [6].

	PW91	PBE	revPBE	revPBE-D3
CO/mica(**A**)	0.35	0.32	0.25	0.45
CO/mica(**B**)	0.24	0.22	0.16	0.34
CO/mica(**C**)	0.16	0.14	0.11	0.45
CO_2/mica(**A**)	0.32	0.30	0.21	0.47
CO_2/mica(**B**)	0.27	0.26	0.19	0.41
CO/Ni-mica(**A**)	3.64	3.62	3.51	3.43
CO/Ni-mica(**B**)	1.44	1.43	1.22	1.30
CO_2/Ni-mica(**A**)	2.28	2.26	2.12	2.16
CO_2/Ni-mica(**B**)	0.98	0.94	0.72	0.80

The difference between the adsorption energies obtained using PW91 and PBE are small, which is not surprising considering that PBE was constructed to mimic PW91.

When using revPBE, however, the adsorption energies are on average about 0.10 eV lower than when using PBE. The trends are similar to those in another study [29], where the functionals PW91, PBE, revPBE and RPBE are tested and their accuracies compared. For the adsorption energy of CO to nickel, rhodium and palladium, the RMS deviation from experimental results using PW91 was found to be -0.78 eV. Using PBE gave -0.67 eV RMS deviation, while revPBE gave -0.39 eV. The results from the testing by Y. Zhang and W. Yang [28] also indicate that revPBE gives more accurate total atomic energies and atomisation energies of molecules for a range of different atoms and molecules. However, as the systems in the mentioned studies are different from the systems considered here, the same conclusion cannot be drawn with certainty in this case. The deviations are also quite systematic, so comparing the adsorption energies of the various configurations will give the same conclusion regardless of which functional is used. It is still likely that revPBE gives slightly more accurate results, and with no added computational cost, so revPBE is the chosen functional for the rest of the calculations.

The effect of the dispersion correction is less systematic and it depends on the system involved to a larger degree. CO and CO_2 are weakly adsorbed on mica, and all these structures have a change in adsorption energies between +0.18 eV and +0.26 eV, which are noticeable changes. These values for adsorption energy change do not include structure CO/mica(**C**), as the geometry changed into structure CO/mica(**A**). For the considerably stronger bound systems with CO and CO_2 on nickel-mica, the changes range between +0.04 eV and +/-0.08 eV. The electrostatic and covalent interactions dominate over weak van der Waals forces, and the dispersion correction can therefore be neglected for these systems. From now on, the dispersion correction will not be included in the calculations.

4.2 Transition metals on mica

My specialisation project reported that nickel adsorbs willingly on the mica surface, with an adsorption energy of 0.71 eV [6]. The nickel-mica surface gave excellent results for CO and CO_2 adsorption, with the adsorption energies stated in section 4.1. To see if other transition metals have the same effect, some attempts were made to place different transition metals on the mica surface. Among these were Ti, Cr, Mn, Fe, Cu, Zn, Pd, Ag and Cd. Unfortunately none of these adsorbed on mica the way that nickel did. Palladium physisorbed with an adsorption energy of 0.16 eV, while the other metals gave even lower adsorption energies, in the magnitude of 0.01 eV.

To explain why nickel is the only metal to adsorb on mica, nickel's electron configuration and density of states were calculated. The electron configuration of the free nickel atoms in a periodic arrangement was found using Mulliken population analysis to be $[Ar]3d^9 4s^1$. The density of states is plotted in figure 4.1.

The plot shows a large density of states at the Fermi level E_F = -4.27 eV, which mostly belongs to the *d* band, and a small part to the *s* band. The large density of states at the Fermi level is probably a reason for the high reactivity of nickel, and why nickel adsorbs stronger to the mica surface than the other transition metals. For the rest of the report, the focus is limited to the 3*d* transition metals Mn, Fe, Co, Ni, Co and Zn.

All the 3*d* transition metals, except zinc, have partially filled *d* subshells in the free element. The filling of the 3*d* subshell follows Hund's rules, namely that the electrons

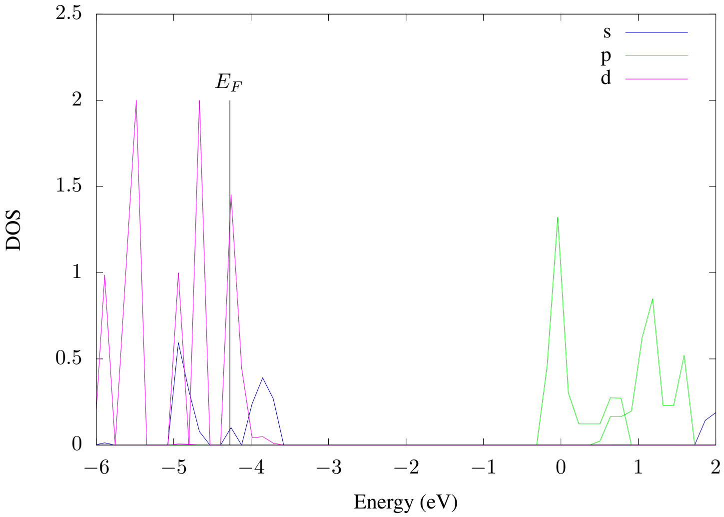

Figure 4.1: The partial DOS for nickel.

will maximise total spin by filling all the orbitals with similar energy before pairing with another electron in a half-filled orbital. According to Hund's rules, manganese should have 5 unpaired electrons, iron 4, cobalt 3, nickel 2, copper 1 and zinc none. As the unpaired electrons are aligned in the ground state, all the metals, except zinc, will have a net spin, making them paramagnetic. To confirm the assumption, calculations of each of the transition metals as free atoms in a periodic slab arrangement were performed spin unrestricted. The results were exactly as expected.

4.3 Metal oxides on mica

To investigate the effect of oxygen on the adsorption properties, metal oxide-mica surfaces were prepared with the metals Mn, Fe, Co, Ni, Cu and Zn. The nickel oxide-mica surface was made by placing an oxygen atom on the nickel-mica surface from the specialisation project [6], and geometry optimising the structure. The other surfaces were made by placing a metal oxide molecule on the mica surface, as none of the other metals adsorbed on mica alone.

The adsorption energy of oxygen on metal-mica is given by [9]

$$E_{\text{ads}} = E(\text{Met-mica}) + \frac{1}{2}E(\text{O}_2) - E(\text{O/Met-mica}). \tag{4.2}$$

The first term on the right is the energy of the metal-mica surface, the second term is one half of the energy of an oxygen gas molecule, and the third term is the energy of the oxygen adsorbed on the metal-mica surface. The adsorption energy represents half the energy required to pull two oxygen atoms off the surface to form an O_2 gas molecule.

The structures of the resulting metal oxide-mica surfaces are depicted in figures 4.2-4.7. In all the figures, the image on the left gives a [010] view of the surface, while the image on the right gives a [001] view of the surface.

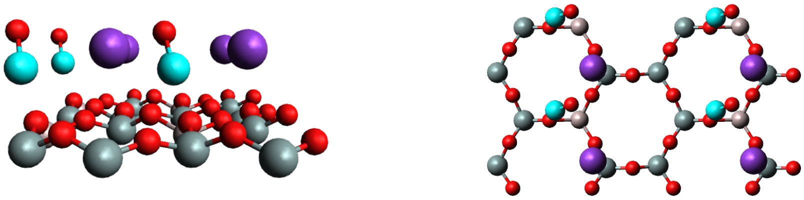

Figure 4.2: The structure of MnO-mica, showing the two topmost layers. 2 × 2 unit cells are shown, and the colour code is the same as in figure 1.2. The manganese atom is coloured aqua blue.

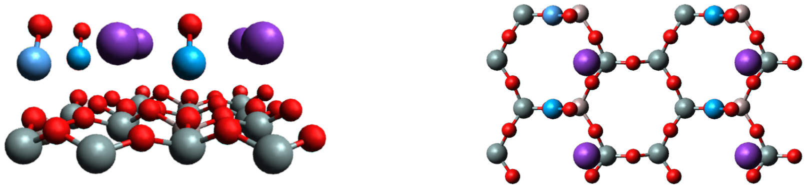

Figure 4.3: The structure of FeO-mica, with iron coloured light blue.

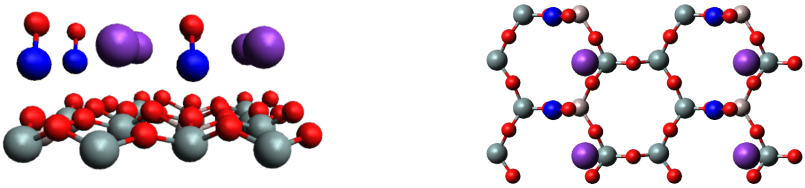

Figure 4.4: The structure of CoO-mica, with cobalt coloured dark blue.

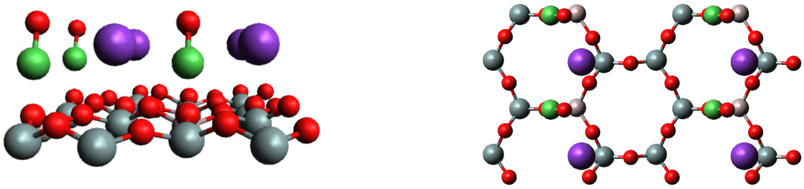

Figure 4.5: The structure of NiO-mica, with nickel coloured green.

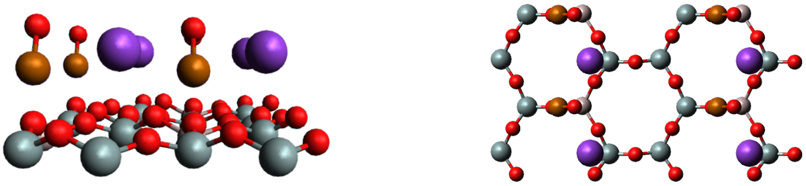

Figure 4.6: The structure of CuO-mica, with copper coloured brown.

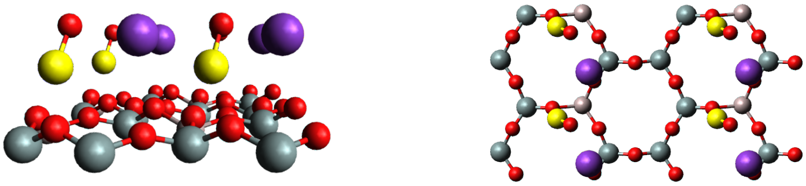

Figure 4.7: The structure of ZnO-mica, with zinc coloured yellow.

The adsorption energies of the top oxygen atom to the metal-mica surfaces and some bond lengths are presented in table 4.2. For CoO-mica, the adsorption energy was not calculated as the Co-mica structure could not be converged with respect to the SCF cycles.

Table 4.2: The calculated adsorption energies of oxygen to all the surfaces, and some bond lengths. M denotes the transition metal atom and O the adsorbed oxygen. K1 and K2 denote the potassium atom in the left and right unit cell, respectively, when looking at the left image of figures 4.2-4.7.

	E_{ads}(eV)	$d_{\text{M-O}}$(Å)	$d_{\text{O-K1}}$(Å)	$d_{\text{O-K2}}$(Å)
MnO-mica	3.36	1.71	2.62	3.66
FeO-mica	3.61	1.68	3.03	3.01
CoO-mica	-	1.68	3.04	3.02
NiO-mica	2.98	1.68	3.12	3.02
CuO-mica	1.64	1.76	3.02	3.04
ZnO-mica	0.68	1.74	3.40	2.63

The oxygen atom bonds mainly to the metal atom on the surface, and weakly to the potassium atoms. Therefore, the adsorption energies of oxygen to the metal-mica surface correlate with known dissociation energies of the metal-oxygen bonds [46].

In all the structures, the potassium, oxygen and metal atoms have formed a distinct layer together, where the oxygen atom is placed on the top and is accessible to react with an adsorbate. The surfaces with Fe, Co, Ni and Cu are fairly similar, with the top oxygen atom placed in such a way that its distance to both potassium atoms is almost equal. The structures with Mn and Zn are slightly different from the others with the top oxygen atom moving closer to one potassium atom, making the structures asymmetric. These differences are clear from the potassium-oxygen bond lengths in table 4.2.

A Bader analysis was performed to find the partial charges of the metal and oxygen atoms on the surface, which are presented in table 4.3.

Table 4.3: The partial charges of the transition metal and the adsorbed oxygen in the metal oxide-mica surfaces. The partial charges are given in the unit e, the elementary charge.

	M(e)	O(e)
MnO-mica	1.030	-1.080
FeO-mica	0.913	-1.006
CoO-mica	0.785	-0.905
NiO-mica	0.674	-0.821
CuO-mica	0.668	-0.804
ZnO-mica	0.978	-1.110

The magnitude of charge transferred between the metal and oxygen atom correlates to some degree with the adsorption energies, with the exception being ZnO-mica. Here, the partial charges deviate from the trend.

4.4 CO_2 adsorption on metal oxide-mica

CO_2 is placed on top of all the metal oxide-mica surfaces. The most stable structures of CO_2 adsorbed on each of the surfaces are depicted in figures 4.8-4.13. In all the figures, the left image gives a [010] view of the surface, the middle image gives a [001] view of the surface, and the rightmost image shows the isolated carbonate-metal group with indicated angles.

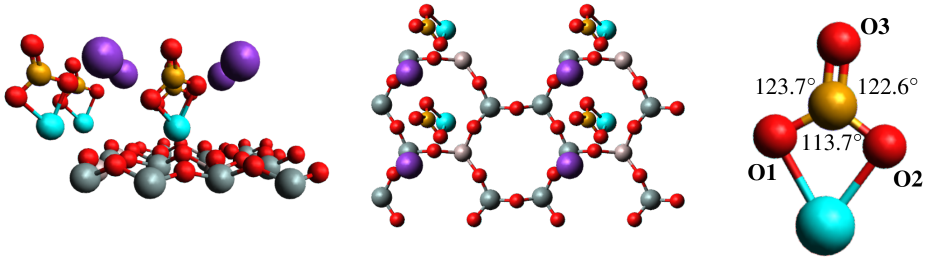

Figure 4.8: The most stable structure of CO_2 adsorbed on MnO-mica, with the carbon atom gold coloured. The numbering of the oxygen atoms indicated here are continued throughout this section.

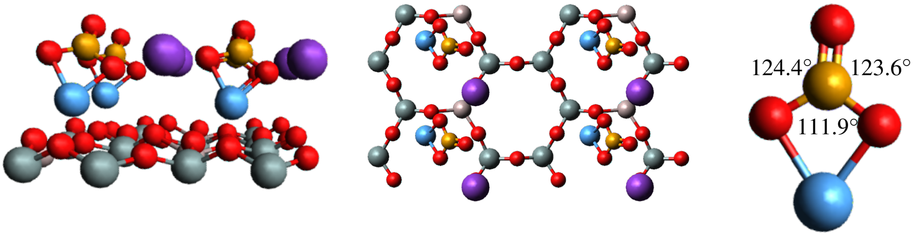

Figure 4.9: CO_2 adsorbed on FeO-mica.

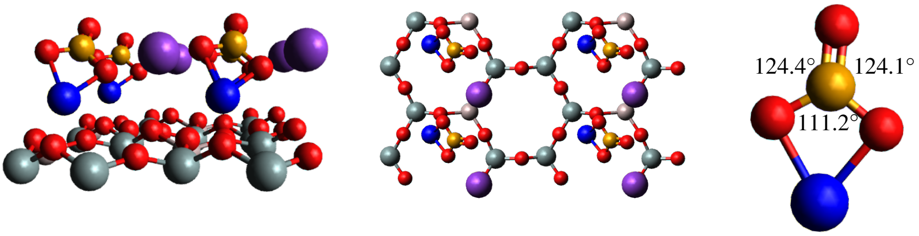

Figure 4.10: CO_2 adsorbed on CoO-mica.

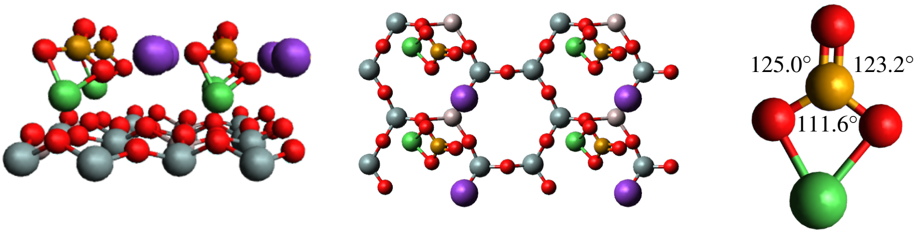

Figure 4.11: CO_2 adsorbed on NiO-mica.

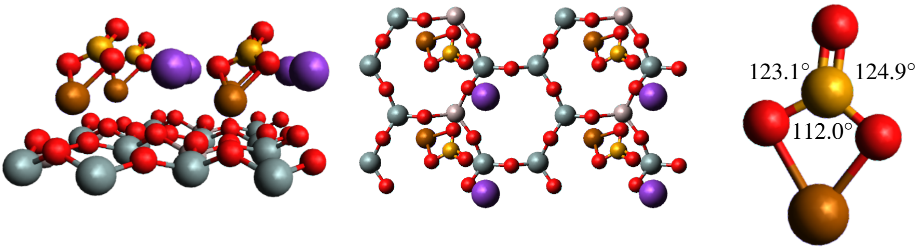

Figure 4.12: CO_2 adsorbed on CuO-mica.

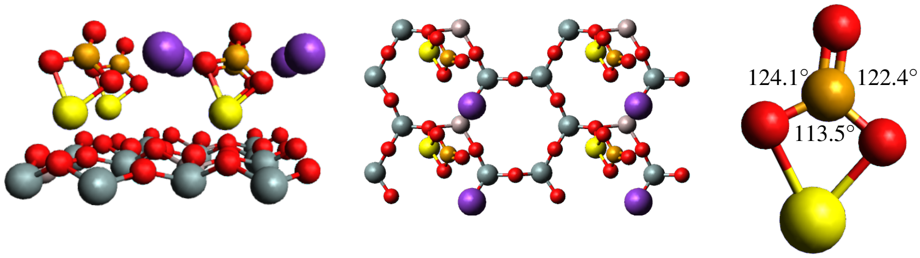

Figure 4.13: CO_2 adsorbed on ZnO-mica.

The adsorption energies of CO_2 to the surface and some bond lengths of all the structures are stated in table 4.4. The adsorption energies were calculated using equation 4.1.

Table 4.4: The adsorption energies of CO_2 to the metal oxide-mica surfaces and some selected bond lengths. O1 denotes the oxygen atom that was originally on the surface, while O2 and O3 denote the oxygen atoms that were a part of the CO_2 molecule.

	E_{ads}(eV)	$d_{\text{C-O1}}$(Å)	$d_{\text{C-O2}}$(Å)	$d_{\text{C-O3}}$(Å)	$d_{\text{M-O1}}$(Å)	$d_{\text{M-O2}}$(Å)
CO_2/MnO-mica	2.11	1.33	1.35	1.27	2.09	2.02
CO_2/FeO-mica	1.33	1.35	1.34	1.25	1.94	2.02
CO_2/CoO-mica	1.34	1.35	1.34	1.25	1.95	1.98
CO_2/NiO-mica	1.10	1.35	1.33	1.26	1.93	2.02
CO_2/CuO-mica	1.65	1.33	1.33	1.25	1.92	2.03
CO_2/ZnO-mica	1.74	1.36	1.34	1.26	1.95	2.03

There is a relatively strong adsorption of CO_2 on all the surfaces, and it seems like a carbonate group has been formed. The adsorption processes may therefore be categorised as chemisorption processes. The surface that gives the largest adsorption energy for CO_2 is MnO-mica, then the bonding gets weaker when going right in the periodic table until reaching NiO-mica. From NiO-mica to ZnO-mica, the adsorption energy increases again.

Carbonate formation is typical for CO_2 chemisorption on surfaces where oxygen is available. Monodentate and bidentate are the most common configurations, but tridentate carbonates have also been proposed [38].

The geometry of the carbonate group is quite similar on all the surfaces, as is evident from the rightmost images in figures 4.8-4.13. The C-O3 bond lengths range from 1.25-1.27 Å, indicating a double or partially double bond. The C-O1 and C-O2 bond lengths (1.33-1.36 Å) indicate single bonds. Because two oxygen atoms bond with the transition metal, the carbonate has a bidentate geometry, similar to the adsorption configuration found on ZnO(10$\bar{1}$0) in a study from 1993 [47]. The carbonate-metal species belong to the C_{2v} point group, and has an almost trigonal planar arrangement. The orientation of the CO_3 group on the surfaces is quite similar in most structures, but on MnO-mica and CuO-mica, it is twisted slightly relative to the other surfaces.

A Bader analysis was conducted to find the partial charges of some of the atoms in all the adsorbed structures. The results are presented in table 4.5.

Table 4.5: The partial charges of the CO_2 molecule isolated, as well as adsorbed on the various surfaces. The structures are ordered from highest to lowest adsorption energy.

	C(e)	O1(e)	O2(e)	O3(e)	M(e)	CO_3(e)
CO_2	1.967	-	-0.984	-0.984	-	-
CO_2/MnO-mica	1.812	-1.098	-1.091	-1.137	1.382	-1.514
CO_2/ZnO-mica	1.843	-1.068	-1.095	-1.139	1.288	-1.459
CO_2/CuO-mica	1.910	-0.977	-1.073	-1.002	0.985	-1.142
CO_2/CoO-mica	1.845	-1.029	-1.127	-1.019	1.157	-1.330
CO_2/FeO-mica	1.856	-1.055	-1.070	-1.121	1.251	-1.390
CO_2/NiO-mica	1.866	-1.000	-1.022	-1.109	1.064	-1.265

When comparing these results with the partial charges of the oxygen and metal atom before CO_2 was adsorbed in table 4.3, it is evident that there is an electron transfer from the metal to the CO_2 molecule during the adsorption. The result is the formation of the negatively charged $CO_3^{\gamma-}$ group, where γ denotes the charge. The general trend is that the magnitude of the charge transfer increases with the strength of the bonding. This is a reasonable result as the electron transfer means stronger interaction between the surface and the adsorbate. The CO_2/CuO-mica structure deviates from the trend.

4.4.1 Potential energy surfaces

In this section, each metal oxide-mica surface is studied more carefully by considering the potential energy surface of its reaction with CO_2. The C-O1 bond length is the coordinate that best measures the distance between the CO_2 molecule and the surface, and is therefore the chosen coordinate for the linear transit calculations.

CO_2 on MnO-mica

The CO_2 adsorption path on the MnO-mica surface was investigated starting with a linear CO_2 molecule far away from the surface, with the initial C-O1 bond length 2.95 Å. The molecule was gradually moved closer to the surface, and the energy was calculated at each step. The result is that the energy decreases the whole way, so there does not seem to be an energy barrier present for the chemisorption. A possible explanation for this is the position of the top oxygen on the MnO-mica surface. According to table 4.2, the oxygen is closer to one potassium atom, with the bond length $d_{\text{O-K1}}$ = 2.62 Å. The distance to the other potassium atom is $d_{\text{O-K2}}$ = 3.66 Å, meaning that the oxygen atom is virtually only bonded to K1. Hence, no bonds need to be broken for CO_2 to adsorb, as the oxygen is still bonded to K1 after the adsorption, with a bond length of 2.71 Å. This process is thus an example of nonactivated carbonate formation, which has been predicted before, for example for CO_2 adsorption on a MgO(100) surface [48].

CO_2 on FeO-mica

The linear transit calculation for the CO_2 adsorption on the FeO-mica surface reveals the existence of an energy barrier. As opposed to the MnO-mica surface, the top oxygen atom on the FeO-mica surface is placed in the middle of the two potassium atoms, and the oxygen is therefore bonded weakly to both of them. For CO_2 to be able to adsorb on the surface, oxygen must break its bond with one of the potassium atoms to make room for the carbonate. As energy is required to break this bond, a barrier must be overcome for the reaction to happen.

The transition state (**TS**) and the two energy minima **A** and **B** are indicated in the energy diagram in figure 4.14.

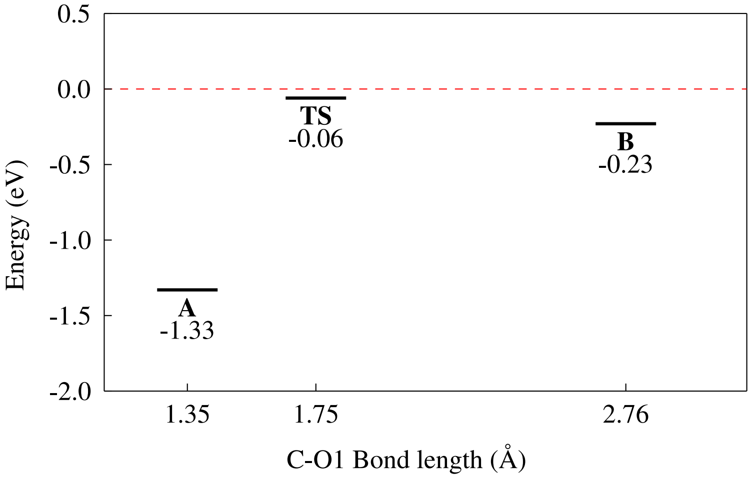

Figure 4.14: A schematic representation of the stationary points of the potential energy surface for CO_2 adsorption on FeO-mica. The points are positioned with respect to the distance between the carbon atom and the oxygen atom on the mica surface. The zero energy is defined as the sum of the energies of the free CO_2 molecule and the FeO-mica surface.

Minimum **A** is the chemisorbed structure depicted in figure 4.9. Minimum **B** represents a physisorbed geometry, with the adsorption energy 0.23 eV and a O2-C-O3 bond angle of 173.3°. It is quite far from the surface, with a C-O1 bond length of 2.76 Å.

The transition state has an adsorption energy of 0.06 eV. It is located closer to the ending point than the starting point on the path, and is therefore termed a *late transition state*. To include one example of the structure at the transition state, the transition state for CO_2 on FeO-mica is depicted in figure 4.15.

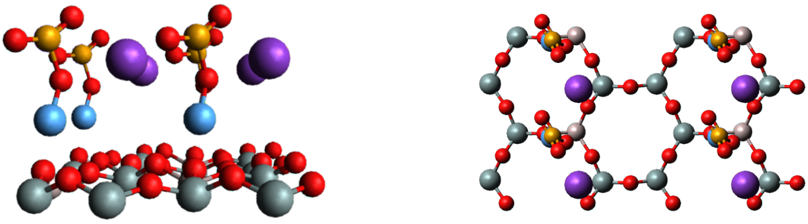

Figure 4.15: The transition state of CO_2 adsorbed on FeO-mica.

At this point, the C-O2 and C-O3 bond lengths are both 1.23 Å, and the O2-C-O3 angle is 142.9°. The CO_2 molecule has changed significantly from its free form, and is on its way to chemisorb as in minima **A**.

According to these results and equation (2.28), the activation energy needed to get from minimum **B** to **A** is E_a = 0.17 eV.

CO_2 on CoO-mica

For CO_2 on CoO-mica, a physisorbed geometry with weak bonding was detected, in addition to the chemisorbed geometry shown in figure 4.10. Hence, there should be an energy barrier for chemisorption. A linear transit calculation indicated that there is a transition state around the C-O1 bond length 1.75 Å, but the calculations were not converged. Due to SCF convergence problems, I was not able to converge the geometry optimisations. Therefore, a reliable value for the activation energy for this structure was not found.

The physisorbed geometry, denoted CO_2/CoO-mica(**B**), has an adsorption energy of 0.17 eV. The O2-C-O3 bond angle is 176.8° and the C-O1 bond length is 2.94 Å, meaning that the CO_2 molecule is less bent and further from the surface than for CO_2/FeO-mica(**B**). This is reasonable as the latter is bonded more strongly to the surface.

CO_2 on NiO-mica

An energy barrier was found for the CO_2 adsorption on NiO-mica as well. In figure 4.16, one transition state (**TS**) and three local minima **A**, **B** and **C** of the potential energy surface are indicated in an energy diagram.

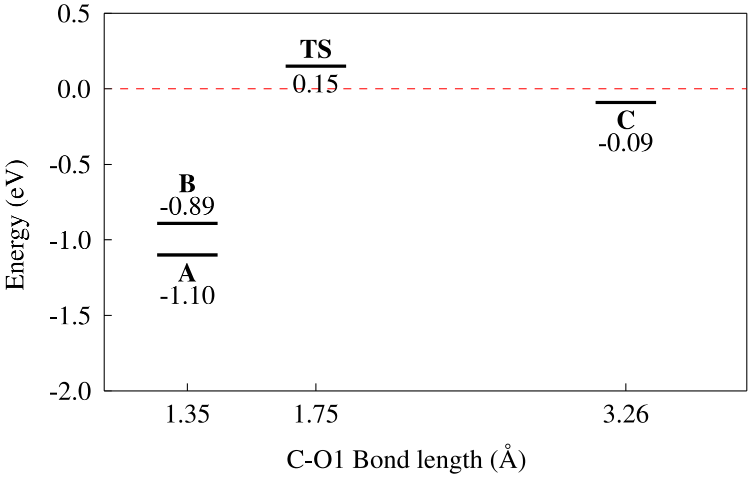

Figure 4.16: A schematic representation of the stationary points of the potential energy surface for CO_2 adsorption on NiO-mica.

Minimum **A** is the most stable structure and is depicted in figure 4.11, while minimum **B** is another chemisorbed adsorption geometry with a slightly higher energy. This structure involves a $CO_3^{\gamma-}$ group like in geometry **A**, but the whole group is oriented differently on the surface. The energy path between these two minima could have been investigated to find another transition state, but the reaction path is complicated and too time consuming for this project. Minimum **C** represents a physisorbed geometry where CO_2 is far from the surface and has a O2-C-O3 angle of 178.5°. The adsorption energy is 0.09 eV, so the geometry is only barely energetically profitable.

The transition state is marked in the diagram with an adsorption energy of -0.15 eV, and a C-O3 bond length of 1.75 Å. As the transition state is located closer to minima **A** and **B** than minimum **C**, it is a late transition state. According to the linear transit calculation, the activation energy needed to get from the physisorbed geometry to the chemisorbed ones is E_a = 0.24 eV.

CO_2 on CuO-mica

The linear transit calculation of CO_2 on CuO-mica indicates that there is an energy barrier for the chemisorption process. The energy diagram is shown in figure 4.17, with the stationary points transition state (**TS**) and three minima **A**, **B** and **C** indicated.

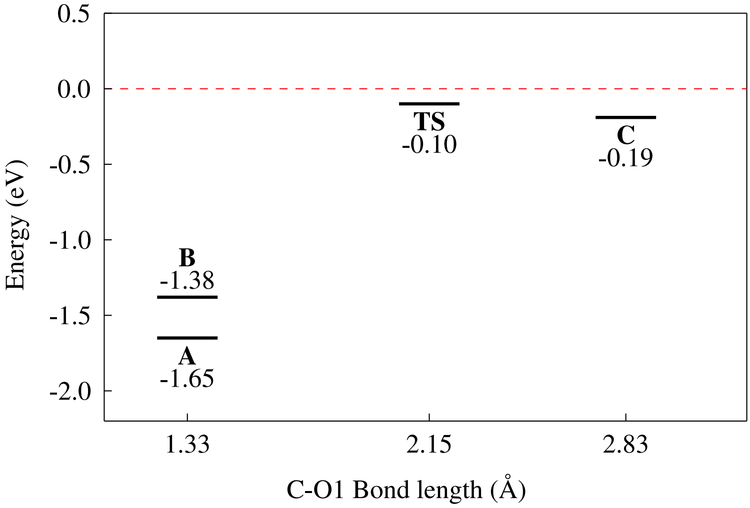

Figure 4.17: A schematic representation of the stationary points of the potential energy surface for CO_2 adsorption on CuO-mica.

Minima **A** and **B** are both chemisorbed structures with a $CO_3^{\gamma-}$ group present on the surface. Minimum **A** is the one considered previously and depicted in figure 4.12, and minimum **B** has a structure with the $CO_3^{\gamma-}$ group rotated slightly, similar to CO_2/NiO-mica(**B**). The reaction path between these points has not been explored. Minimum **C** is a structure where CO_2 is weakly physisorbed to the surface, with an adsorption energy of 0.19 eV and O2-C-O3 angle of 175.6°.

At the transition state, CO_2 has an adsorption energy of 0.10 eV. It is closer to minimum **C** than **A** and **B**, making it an *early transition state*. The activation energy is E_a =

0.09 eV, which is smaller than for NiO-mica and FeO-mica. This indicates that CO_2 is more easily adsorbed on CuO-mica.

CO_2 on ZnO-mica

A linear transit calculation of CO_2 on ZnO-mica indicates that there is no energy barrier for adsorption. The energy seems to go steadily downhill, and CO_2 chemisorbs even with an initial C-O1 bond length of 2.95 Å in the geometry optimisation. An explanation for this is the structure of ZnO-mica, depicted in figure 4.13, which is asymmetric like MnO-mica. As mentioned before, the asymmetric structure makes it easier for CO_2 to swoop in without requiring any bond breaking, thus avoiding energy barriers.

To summarise, the surfaces that give an energy barrier for CO_2 chemisorption are FeO-mica, CoO-mica, NiO-mica and CuO-mica. These are the same surfaces where the top oxygen atom is positioned in the middle of the two potassium atoms. This is in agreement with the explanation that the breaking of the O-K bond is the reason for the energy barrier.

CO_2 chemisorption on the surfaces MnO-mica and ZnO-mica, where there is no energy barrier, have the two largest adsorption energies. The CO_2/CuO-mica(**A**) structure has the third largest adsorption energy, and the smallest activation energy, 0.09 eV, of the remaining surfaces. CO_2 chemisorption on NiO-mica, which has the smallest adsorption energy, has the largest activation energy of 0.24 eV. Consequently, the adsorption energy for chemisorption seems to correlate with the activation energy. None of the activation barriers are unreasonably high. The highest activation energy of 0.24 eV gives a relatively slow, but not impossible, chemisorption of CO_2 to NiO-mica.

It is important to note that the energy diagram is based on a one dimensional energy plot, so the position and energy of the transition states are therefore not particularly accurate. The main features of the diagrams are still considered to be close to reality. Additionally, the magnitudes of the activation energies for the different surfaces compared to each other should be reliable.

Ideally, the transition states should have been verified by performing frequency calculations to ensure that there is exactly one imaginary frequency at this point. Such calculations were attempted, but unfortunately they gave frequencies of unreasonable magnitudes that were not thought to be reliable.

4.4.2 Density of states

To investigate how the density of states is affected by the adsorbed CO_2 molecule, the density of states is plotted for the adsorbed structures together with the surface without CO_2. Plots are made for the most stable chemisorbed adsorption site for each surface, and for the physisorbed adsorption sites that were found. The density of states for the free CO_2 molecule is plotted in figure 4.18, for comparison. The most stable surfaces are denoted with an **A** in parenthesis, and the physisorbed structures with a **B** or **C**, consistent with the notation in the energy diagrams.

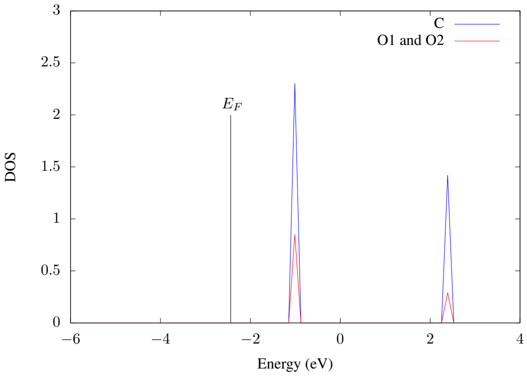

Figure 4.18: Partial density of states for the free CO_2 molecule.

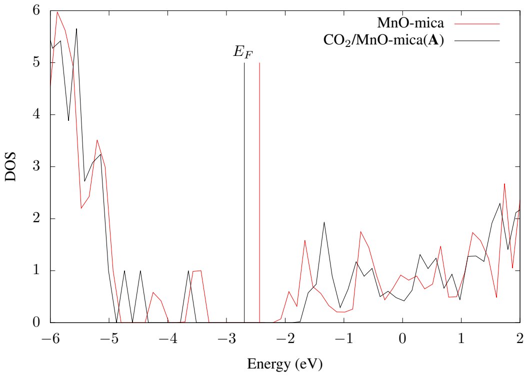

Figure 4.19: Density of states for CO_2/MnO-mica(**A**).

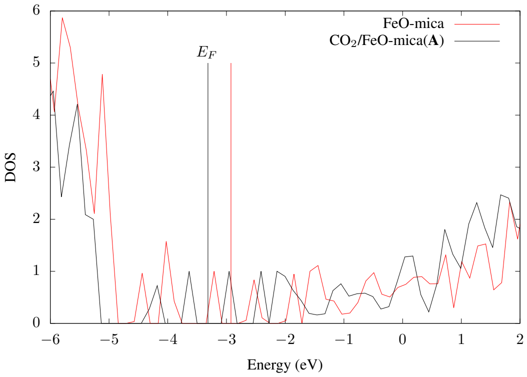

Figure 4.20: Density of states for CO_2/FeO-mica(**A**).

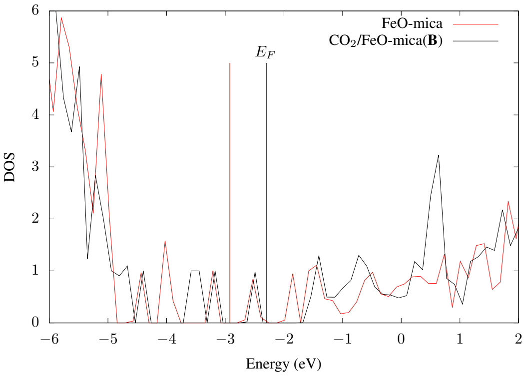

Figure 4.21: Density of states for CO_2/FeO-mica(**B**).

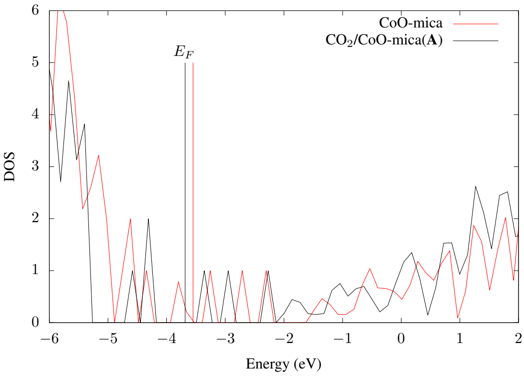

Figure 4.22: Density of states for CO_2/CoO-mica(**A**).

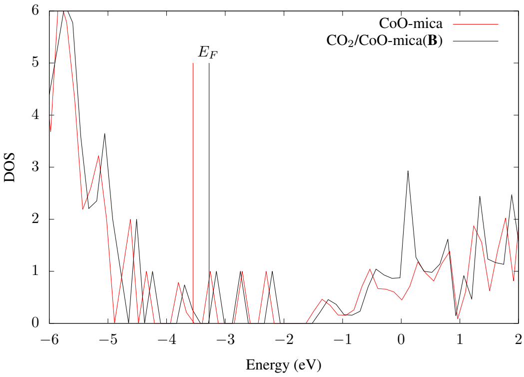

Figure 4.23: Density of states for CO_2/CoO-mica(**B**).

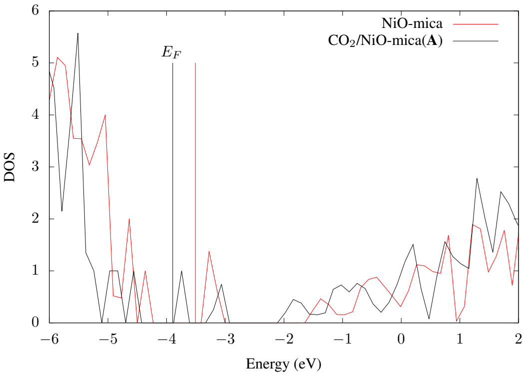

Figure 4.24: Density of states for CO$_2$/NiO-mica(**A**).

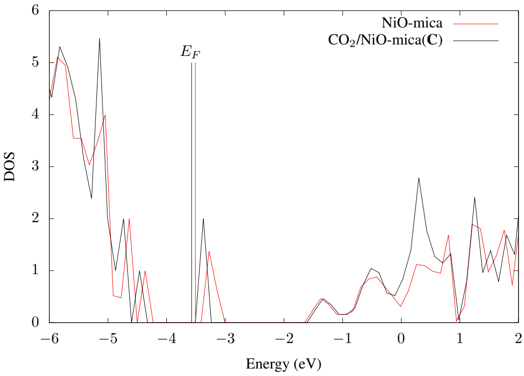

Figure 4.25: Density of states for CO$_2$/NiO-mica(**C**).

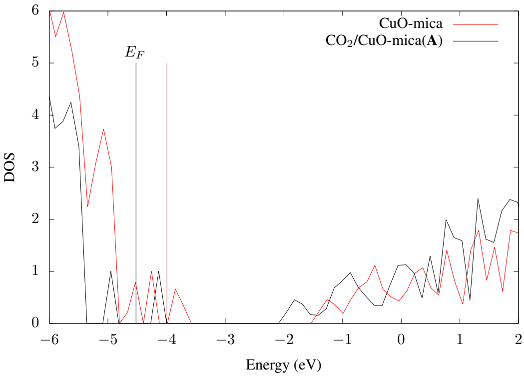

Figure 4.26: Density of states for CO$_2$/CuO-mica(**A**).

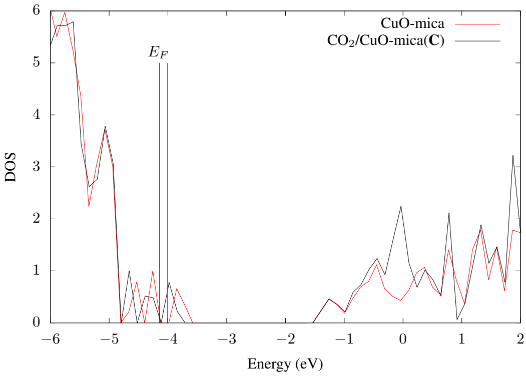

Figure 4.27: Density of states for CO_2/CuO-mica(**C**).

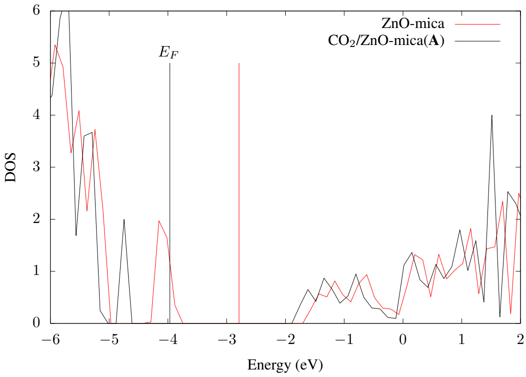

Figure 4.28: Density of states for CO_2/ZnO-mica(**A**).

It is clear that the density of states for all the chemisorbed structures is significantly altered from the metal oxide-mica surface, and new bands have formed. This was expected as the structure of the surface has been rearranged. For the physisorbed structures, the density of states for the surface with CO_2 is almost perfectly overlapping with the density of states for the one without, except at energies around 0 eV or between 0 and 1 eV. Here, the CO_2 contribution adds to the density of states. The density of states for the free CO_2 molecule has shifted slightly after adsorption. Apart from this, there is hardly any large changes in the DOS. The exception from this observation is CO_2/FeO-mica(**B**), where the density of states is altered more after adsorption than for the other physisorbed structures. This is also the physisorbed structure with the highest adsorption energy, namely 0.23 eV, and where the CO_2 molecule is most bent after adsorption.

To get an overview of the Fermi energies and band gaps for the structures, they are summarised in table 4.6.

Table 4.6: The Fermi energies and band gaps for the surfaces without CO_2, and for the adsorption geometries with chemisorbed and physisorbed CO_2. For MnO-mica and FeO-mica, no physisorbed structure was found.

			With CO_2(**A**)		With CO_2(**B**/**C**)	
	E_F(eV)	E_g(eV)	E_F(eV)	E_g(eV)	E_F(eV)	E_g(eV)
MnO-mica	-2.44	1.40	-2.70	1.88	-	-
FeO-mica	-2.92	0.56	-3.32	0.59	-2.29	0.90
CoO-mica	-3.55	0.41	-3.68	0.92	-3.27	0.41
NiO-mica	-3.51	1.06	-3.90	0.78	-3.57	1.09
CuO-mica	-4.01	0.40	-4.52	0.87	-4.14	0.37
ZnO-mica	-2.79	2.28	-3.97	2.94	-	-

For all the structures, the Fermi energy is located inside the band gap, which makes the structures insulators or semiconductors. For CO_2/FeO-mica(**B**), CO_2/CoO-mica(**B**), CO_2/NiO-mica(**A**) and CO_2/CuO-mica(**C**), the Fermi energy is just at the edge of the band gap.

4.5 CO adsorption on metal oxide-mica

The adsorption of CO on the metal oxide-mica surfaces was studied in a similar fashion as with CO_2. Two energetically favoured adsorption sites were found for all the surfaces, the most stable ones considered first. The most stable geometries for each surface are depicted in figures 4.29-4.34.

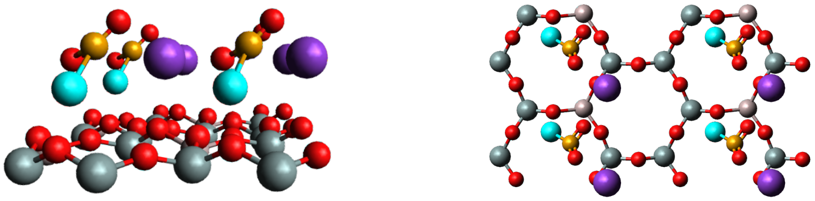

Figure 4.29: CO adsorbed on MnO-mica.

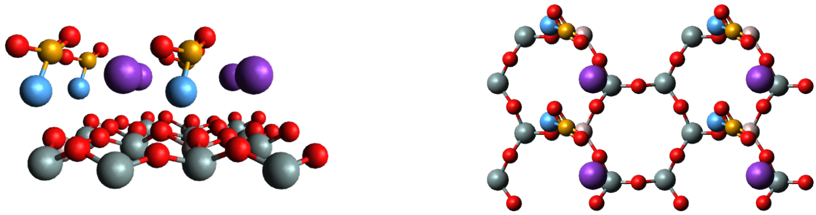

Figure 4.30: CO adsorbed on FeO-mica.

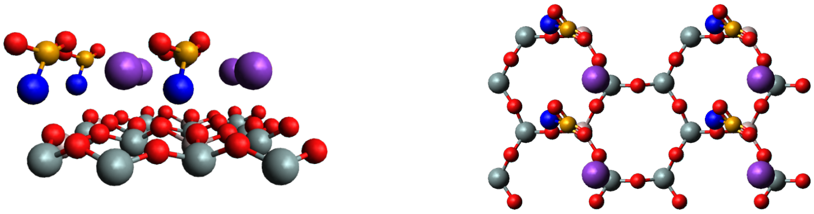

Figure 4.31: CO adsorbed on CoO-mica.

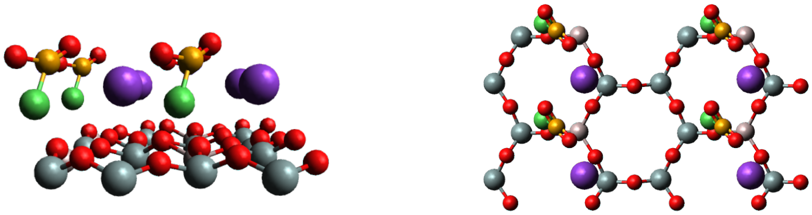

Figure 4.32: CO adsorbed on NiO-mica.

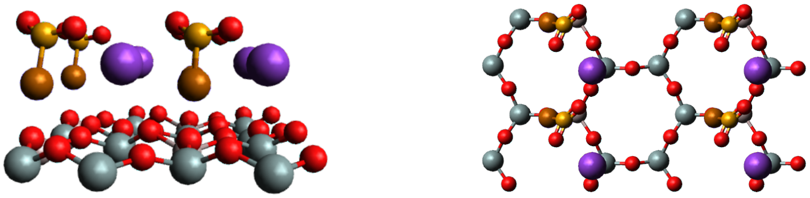

Figure 4.33: CO adsorbed on CuO-mica.

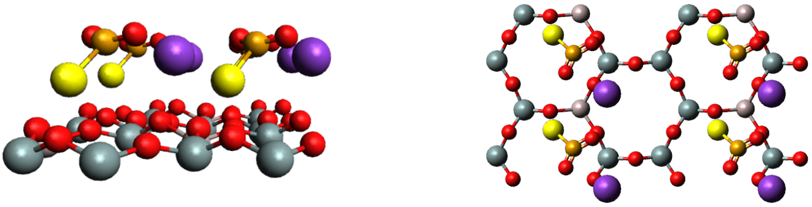

Figure 4.34: CO adsorbed on ZnO-mica.

The adsorption energies and some geometrical parameters of the structures are stated in table 4.7. They are denoted CO/MnO-mica(**A**) etc.

Table 4.7: The adsorption energies of CO to the metal oxide-mica surfaces and some bond lengths. O1 denotes the oxygen that was originally on the surface, while O2 denotes the oxygen in the CO molecule. M denotes the transition metal.

	E_{ads}(eV)	$d_{\text{C-O1}}$(Å)	$d_{\text{C-O2}}$(Å)	$d_{\text{M-C}}$(Å)	∠O1-C-O2(°)
CO/MnO-mica(**A**)	1.26	1.32	1.24	2.00	128.6
CO/FeO-mica(**A**)	1.58	1.32	1.23	1.84	135.7
CO/CoO-mica(**A**)	2.08	1.32	1.24	1.79	135.8
CO/NiO-mica(**A**)	2.53	1.29	1.23	1.81	140.2
CO/CuO-mica(**A**)	2.32	1.24	1.27	1.95	136.8
CO/ZnO-mica(**A**)	2.20	1.26	1.25	2.11	133.8

It is clear that a bent CO_2 species has formed on all the surfaces. The surfaces are significantly altered after adsorption and the adsorption energies are relatively large. The adsorptions are therefore categorised as chemisorption processes. In all the structures, the C-O2 bond lengths have been elongated to 1.23-1.27 Å from 1.14 Å in the free CO molecule. The bonds are also longer than the C-O bond lengths of a free, linear CO_2 molecule, which are 1.17 Å. After comparing the bond lengths and angles of CO/NiO-mica(**A**) in table 4.7 with the same values of CO_2/Ni-mica(**A**) from reference [6], it seems like these structures are virtually identical, as expected.

Although all the structures have the bent CO_2 complex in common, the orientation of the complex, and the position of the potassium atom are different on each surface. The two structures that stand out the most are CO/MnO-mica(**A**) and CO/ZnO-mica(**A**), where the M-C bond lengths are the longest and the CO_2 species are the most bent. This might be related to the asymmetric structures of MnO-mica and ZnO-mica.

A charge transfer analysis was conducted for the surfaces with adsorbed CO, with the results listed in table 4.8.

Table 4.8: The partial charges of the free CO molecule, and CO adsorbed on the metal oxide-mica surfaces. The notation is the same as before. The structures are ordered from large to small O1-C-O2 angle.

	C(e)	O1(e)	O2(e)	CO_2(e)	M(e)	∠O1-C-O2(°)
CO	1.110	-	-1.110	-	-	-
CO/NiO-mica(**A**)	1.359	-0.956	-1.060	-0.657	0.521	140.2
CO/CuO-mica(**A**)	1.340	-1.051	-0.996	-0.707	0.565	136.8
CO/CoO-mica(**A**)	1.265	-0.984	-1.090	-0.809	0.656	135.8
CO/FeO-mica(**A**)	1.299	-0.991	-1.084	-0.776	0.730	135.7
CO/ZnO-mica(**A**)	1.367	-1.110	-1.086	-0.829	0.720	133.8
CO/MnO-mica(**A**)	1.116	-1.099	-1.115	-1.098	1.029	128.6

It is known that electron transfer from a surface to a CO_2 molecule leads to the formation of a bent $CO_2^{\delta-}$ species, where δ is the magnitude of the charge. The larger the electron transfer, the more bent is the molecule, and the larger is the adsorption energy of CO_2 to the surface [38, 49]. It is already observed that a bent CO_2 species has formed on all the surfaces, and the partial charges confirm that they are negatively charged. Additionally, there is a clear correlation between the O1-C-O2 angle and the charge of the $CO_2^{\delta-}$ moiety.

There is an inverse correlation between the adsorption energies of CO and CO_2 to the metal oxide-mica surfaces, which is evident from comparing table 4.4 with 4.7. The NiO-mica surface, which bonds the strongest to CO, bonds weakest to CO_2. The opposite is true for MnO-mica. As opposed to CO_2 adsorption on the metal oxide-mica surfaces, where the adsorbate gains negative charge from the surface, CO here gains positive charge from the surface. I. e., there is an electron transfer from the CO molecule to the surface. The electronegativities of the metals follow the same trends as the CO adsorption to a certain degree, meaning that the metal with the smallest electronegativity, which is Mn, bonds weakest with CO, but strongest with CO_2. This could suggest that the ability of the metal to bond to the adsorbate together with oxygen depends on its ability to attract/repel negative charge, and explain the inverse correlation between the adsorption energies for CO_2 and CO.

The magnitude of the electron transfer between CO and the surface seems to be rather arbitrary, as the CO molecule does not play an important role on its own in the adsorbed structure. The partial charge of the $CO_2^{\delta-}$ moiety, however, increases in magnitude for decreasing adsorption energy of the CO molecule, on the whole. For CO_2 adsorption to a metal-mica surface, the adsorption energy would increase with the magnitude of the partial charge. It seems that the easier it is to remove the CO_2 molecule from this structure, the harder it is to remove the CO molecule from the same structure.

The density of states for the free CO molecule is plotted in figure 4.35, and the density of states for all the adsorbed geometries are plotted in figures 4.36-4.41. The partial density of states for the carbon atom (C), the oxygen atom on the top of the surface (O1) and the oxygen atoms in the CO molecule (O2) are included.

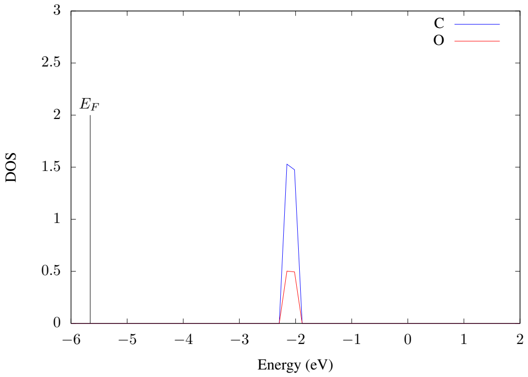

Figure 4.35: The density of states for the free CO molecule.

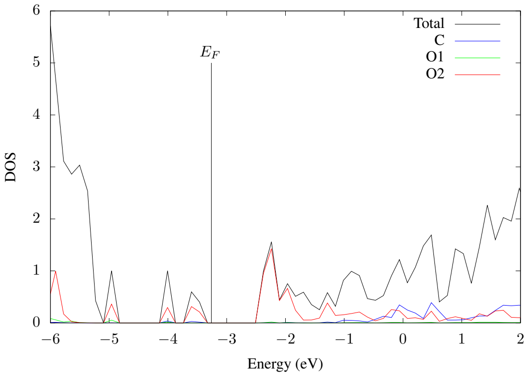

Figure 4.36: Density of states for CO/MnO-mica(**A**).

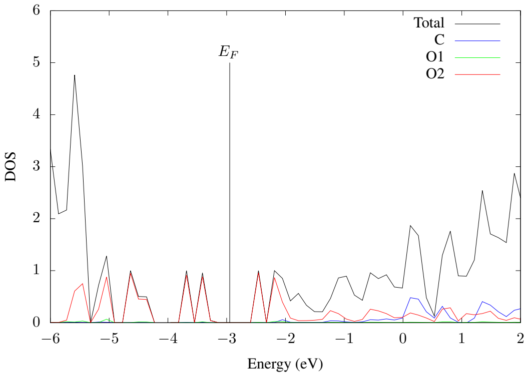

Figure 4.37: Density of states for CO/FeO-mica(**A**).

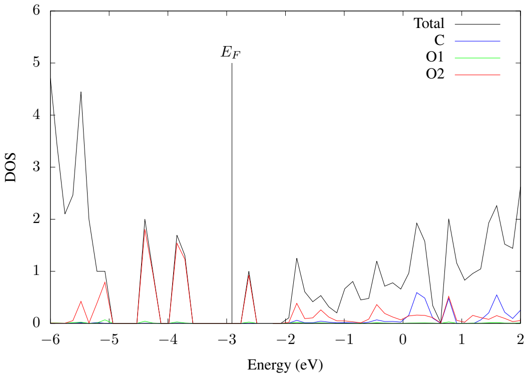

Figure 4.38: Density of states for CO/CoO-mica(**A**).

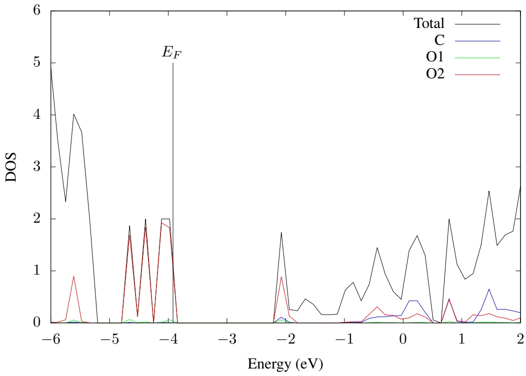

Figure 4.39: Density of states for CO/NiO-mica(**A**).

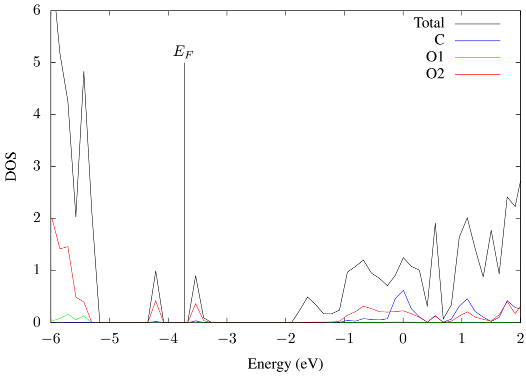

Figure 4.40: Density of states for CO/CuO-mica(**A**).

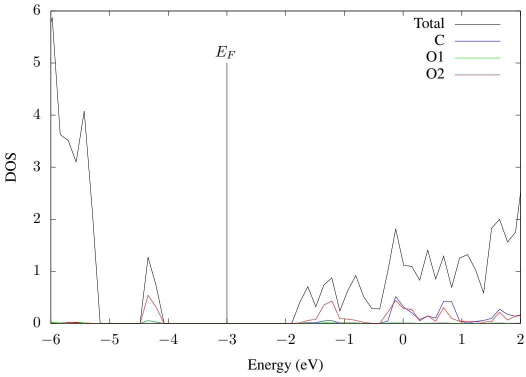

Figure 4.41: Density of states for CO/ZnO-mica(**A**).

The most noticeable feature of the density of states plots is the sizeable contribution from the oxygen atom in the adsorbed CO around the band gap. In all the cases, the CO contribution is altered from that in the free CO molecule, which is typical when the adsorption is strong.

The Fermi energies and band gaps are stated in table 4.9.

Table 4.9: Fermi energies and band gaps for CO adsorbed on metal oxide-mica surfaces.

	E_F(eV)	E_g(eV)
CO/MnO-mica(**A**)	-3.26	1.02
CO/FeO-mica(**A**)	-3.30	0.93
CO/CoO-mica(**A**)	-2.91	1.05
CO/NiO-mica(**A**)	-3.92	1.91
CO/CuO-mica(**A**)	-3.72	0.69
CO/ZnO-mica(**A**)	-3.00	2.39

The Fermi energies are located in the band gap for all the structures, indicating that they are insulators or semiconductors.

4.5.1 Alternative adsorption site

It turns out that there is another adsorption geometry with a lower adsorption energy, that is equivalent for all the surfaces, with CO bonding to the metal atom through carbon, without forming a CO_2 species. An example of this adsorption geometry for CO on MnO-mica, from now on denoted as CO/MnO-mica(**B**), is depicted in figure 4.42. On the left, a [100] view of the surface is pictured, and on the right, a [001] view.

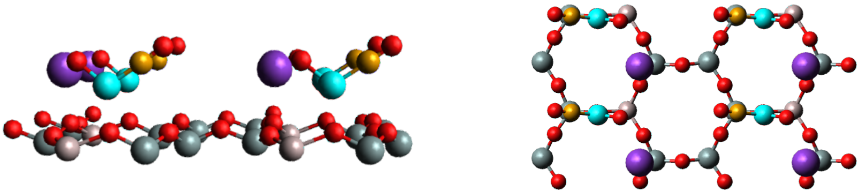

Figure 4.42: The second most stable structure of CO adsorbed on MnO-mica.

An equivalent structure exists for all the surfaces. The adsorption energies of CO and some bond lengths of these structures are stated in table 4.10.

The preferential bonding of CO with the metal through carbon rather than oxygen is evident, and is predicted in other studies [50, 51]. The C-O bond length is elongated from 1.14 Å to 1.16-1.18 Å in the adsorbed structures. The metal-oxygen bond is also elongated after CO is adsorbed for all the cases. The metal and oxygen atoms both shift during the adsorption, even though the surface is not altered to the same extent as it is for geometry **A**. It is therefore reasonable that the adsorption energies are lower.

The pattern for the adsorption energies is similar to that for oxygen on the metal-mica surfaces, stated in table 4.2. The two adsorption processes have in common that the

Table 4.10: The adsorption energies of CO to the metal oxide-mica surfaces and some bond lengths for the second most stable structure. O1 denotes the oxygen that was originally on the surface, while O2 denotes the oxygen in the CO molecule. M denotes the transition metal.

	E_{ads}(eV)	$d_{\text{C-O2}}$(Å)	$d_{\text{C-M}}$(Å)	$d_{\text{M-O1}}$(Å)
CO/MnO-mica(**B**)	1.11	1.18	1.81	1.67
CO/FeO-mica(**B**)	1.28	1.17	1.87	1.72
CO/CoO-mica(**B**)	1.36	1.17	1.83	1.70
CO/NiO-mica(**B**)	0.97	1.17	1.83	1.73
CO/CuO-mica(**B**)	0.90	1.16	1.86	1.80
CO/ZnO-mica(**B**)	0.28	1.16	2.19	1.77

adsorbate bonds almost exclusively to the metal atom, and that electrons are transferred from the adsorbate to the surface. This might be the reason for the similarity in their trends.

4.5.2 Energy diagram for CO on MnO-mica

There should be an activation barrier between the two adsorbed structures, which is investigated for one selected surface, namely CO adsorbed on MnO-mica. When the structure **B** moves towards **A**, the C-O1 bond length is the coordinate that systematically decreases. Therefore, the linear transit calculation was conducted with respect to the C-O1 bond length. The energy diagram for the system is depicted in figure 4.43.

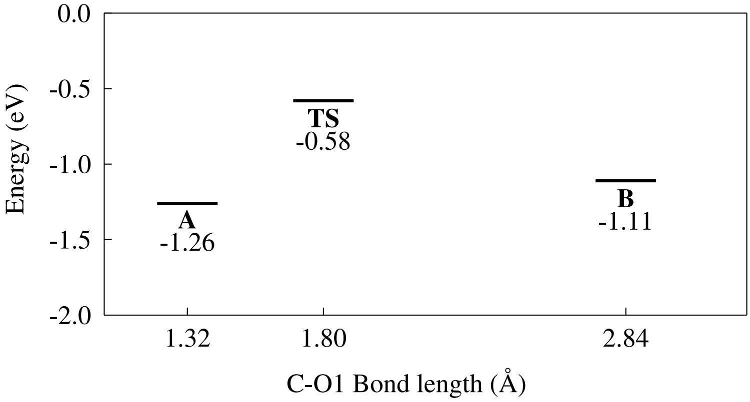

Figure 4.43: A schematic representation of the energy path between minima **A** and **B** for CO adsorption on MnO-mica. The zero energy is defined as the sum of the energies of the free CO molecule and the MnO-mica surface.

The two energy minima indicated in the energy diagram, **A** and **B**, are depicted in figures 4.29 and 4.42, respectively. To get from structure **B** to the slightly more stable structure **A**, the transition state (**TS**) must be passed, with an activation energy of E_a = 0.53 eV. With this sizeable energy barrier, the reaction rate of the structure going from **B** to **A** is particularly slow. The structure at the transition state is shown in figure 4.44.

Figure 4.44: The transition state of CO adsorbed on MnO-mica.

Based on the C-O1 bond length of 1.80 Å, the transition state is closer to the ending point than the starting point, which makes it a late transition state. Both the C-O2 bond and M-O1 bond have elongated from minimum **B**, to 1.19 Å and 1.76 Å, respectively, and the structure is on its way to minimum **A**.

5 | Conclusion

5.1 Concluding remarks

A DFT study was conducted to examine the adsorption of CO_2 and CO to six different metal oxide-mica surfaces, with the metals being the $3d$ transition metals Mn, Fe, Co, Ni, Co and Zn. It was found that both molecules chemisorb on all the surfaces.

For CO_2 adsorption, the most stable adsorption geometry on each surface involves the formation of a bidentate carbonate group, where two of the oxygen atoms bond to the metal atom. A Bader charge analysis showed that the charge of the $CO_3^{\gamma-}$ species increases in magnitude with increasing adsorption energy. The most favourable surface for CO_2 adsorption is the MnO-mica surface, with the adsorption energy E_{ads} = 2.11 eV and no activation barrier. As the adsorption energy for chemisorption decreases, the activation energy increases, making the chemisorption reaction slower. However, with the magnitudes of activation energies found, it is not unlikely that the CO_2 molecule is able to overcome the barrier for all the surfaces, even for NiO-mica, which has the highest activation energy of 0.24 eV.

CO adsorption gives two stable minima on all surfaces. The most stable adsorption geometry involves the formation of a bent, negatively charged $CO_2^{\delta-}$ moiety. The negative charge of the moiety increases the more bent the molecule becomes. For CO adsorption, the NiO-mica surface gives the highest adsorption energy E_{ads} = 2.53 eV. The general trend for the adsorption energies is virtually opposite as that for CO_2 adsorption, which might be related to the direction of the electron transfer between the adsorbate and the metal.

An alternative adsorption site with lower adsorption energies was found for CO adsorption, where CO bonds to the metal through the carbon atom without forming a CO_2 species with the oxygen atom. An equivalent adsorption site exists for all the surfaces. The energy path between the two adsorption sites was investigated for MnO-mica, and an activation energy of 0.53 eV to get from the least stable site to the most stable site was found. Namely, this reaction is extremely slow.

According to these results, the doping of metal oxides on mica seems to improve the adsorption of both CO and CO_2 considerably. When including the results from my specialisation project, the best surface in total for CO adsorption is Ni-mica, with the adsorption energy E_{ads} = 3.51 eV. For CO_2 adsorption, Ni-mica is marginally better than MnO-mica, with an adsorption energy of E_{ads} = 2.12 eV versus 2.11 eV. However, the difference is too small to separate between them with the level of accuracy for this method.

5.2 Further work

The further work on this topic should include testing more transition metals, for example investigate the trends down a row in the periodic table. Additionally, the potential energy surfaces of the systems should be studied more thoroughly. This includes locating a transition state between the two minima for all the CO adsorption surfaces, as well as considering other reaction paths to the chemisorbed minimum.

All the calculations were run spin unrestricted, and the spins for all the surfaces were calculated. Some interesting spin values were found for some of the surfaces, but as spins were not in focus in this thesis, the values were not presented or explored further. For the metal oxide-mica surfaces with and without adsorbed CO_2, all the spins were the same as the respective free transition metal. With adsorbed CO, however, the spin was reduced for some of the surfaces, for both minima **A** and **B**. This might be interesting to study for potential further work.

Bibliography

[1] Core Writing Team, R.K. Pachauri and L.A. Meyer. *Climate Change 2014: Synthesis Report. Contribution of Working Groups I, II and III to the Fifth Assessment Report of the Intergovernmental Panel on Climate Change*. IPCC, 2014.

[2] Carbon Capture and storage Association. `http://www.ccsassociation.org/why-ccs/tackling-climate-change/`. Accessed: 2018-12-16.

[3] H. Hemmen et al. X-ray Studies of Carbon Dioxide Intercalation in Na-Fluorohectorite Clay at Near-Ambient Conditions. *Langmuir*, 28(3):1678-1682, 2012.

[4] A. Botan et al. Carbon Dioxide in Montmorillonite Clay Hydrates: Thermodynamics, Structure, and Transport from Molecular Simulation. *J. Phys. Chem C*, 114(35):14962-14969, 2010.

[5] K. G. Bhattacharyya. Adsorption of Carbon Dioxide on Mica Surfaces. *Langmuir*, 5(5):1155-1162, 1989.

[6] S. U. Sundlisæter. Adsorption of CO and CO_2 on mica and nickel-mica surfaces. 2018 (Unpublished).

[7] T. L. Thompson, O. Diwald and and J. T. Yates. CO2 as a Probe for Monitoring the Surface Defects on TiO2(110) - Temperature-Programmed Desorption. *J. Phys. Chem. B*, 107(48):11700-11704, 2003.

[8] Y. Wang et al. CO2 Activation by ZnO through the Formation of an Unusual Tridentate Surface Carbonate. *Angew. Chem. Int. Ed. Engl.*, 46(29):5624-7, 2007.

[9] D. S. Sholl and J. A. Steckel. *Density Functional Theory - A practical introduction*. Wiley, 2009.

[10] C. Kittel. *Introduction to solid state physics*. Wiley, 2005.

[11] P. C. Hemmer. *Faste stoffers fysikk*. Tapir forlag, 1987.

[12] E. W. Radoslowc. The Structure of Muscovite, $KAl_2(Si_3Al)O_{10}(OH)_2$. *Acta Cryst.*, 13:919-932, 1930.

[13] A. N. Rudenko, F. J. Keil, M. I. Katsnelson, and A. I. Lichtenstein. Graphene adhesion on mica: Role of surface morphology. *Physical Review B*, 83(4):045409, 2011.

[14] E. Schrödinger. Quantisierung als eigenwertproblem. *Annalen der physik*, 385(13):361-386, 1926.

[15] M. Born and R. Oppenheimer. Zur quantentheorie der molekeln. *Annalen der Physik*, 389(20):457-484, 1927.

[16] D. R. Hartree. The wave mechanics of an atom with a non-coulomb central field, part 1, theory and methods. *Mathematical Proceedings of the Cambridge Philosophical Society*, 24(1):89-110, 1928.

[17] W. Pauli. Über den Zusammenhang des Abschlusses der Elektronengruppen im Atom mit der Komplexstruktur der Spektren. *Zeitschrift für Physik*, 31(1):765-783, 1925.

[18] V. Fock. Selfconsistent field mit austausch für natrium. *Zeitschrift für Physik*, 62(11):795-805, 1930.

[19] J. C. Slater. The theory of complex spectra. *Physical Review*, 34(10):1293, 1929.

[20] J. M. Thijssen. *Computational physics*. Cambridge University Press, 1999.

[21] P. Hohenberg and W. Kohn. Inhomogeneous electron gas. *Physical Review*, 136(3B):B864, 1964.

[22] W. Kohn and J. L. Sham. Self-Consistent Equations Including Exchange and Correlation Effects. *Physical Review*, 140(4A):A1133, 1965.

[23] R. O. Jones. Density functional theory: Its origins, rise to prominence, and future. *Reviews of Modern Physics*, 87(3):897, 2015.

[24] L. H. Thomas. The calculation of atomic fields. *Proceedings of the Cambridge Philosophical Society*, 23(5):542, 1927.

[25] E. Fermi. Un Metodo Statistico per la Determinazione di alcune Priopriettà dell'Atomo. *Rend. Accad. Naz. Lincei.*, 6:602-607, 1927.

[26] J. P. Perdew et al. Atoms, molecules, solids, and surfaces: Applications of the generalized gradient approximation for exchange and correlation. *Physical review B*, 46(11):6671-6687, 1992.

[27] J. P. Perdew, K. Burke and M. Ernzerhof. Generalized Gradient Approximation Made Simple. *Physical Review Letters*, 77(18):3865-3868, 1996.

[28] Y. Zhang and W. Yang. Comment on "Generalized Gradient Approximation Made Simple". *Physical Review Letters*, 80(4):890, 1998.

[29] B. Hammer, L. B. Hansen and J. K. Nørskov. Improved adsorption energetics within density-functional theory using revised Perdew-Burke-Ernzerhof functionals. *Physical review B*, 59(18):7413, 1999.

[30] S. Grimme. Semiempirical GGA-Type Density Functional Constructed with a Long-Range Dispersion Correction. *Journal of Computational Chemistry*, 27(15):1787-1799, 2006.

[31] S. Grimme, J. Antony, S. Ehrlich and H. Krieg. A consistent and accurate ab initio parametrization of density functional dispersion correction (DFT-D) for the 94 elements H-Pu. *The Journal of Chemical Physics*, 132(15):154104, 2010.

[32] F. Bloch. Über die Quantenmechanik der Elektronen in Kristallgittern. *Zeitschrift für Physik*, 52(7):555-600, 1929.

[33] H. J. Monkhorst and J. D. Pack. Special points for Brillonin-zone integrations. *Physical Review*, 13(12):5188-5192, 1976.

[34] J. C. Slater. Atomic shielding constants. *Physical Review*, 36(1):57-64, 1930.

[35] A. R. Leach. *Molecular Modelling, Principles ans applications*. Pearson, 1996.

[36] J. I. Steinfeld, J. S. Francisco and W. L. Hase. *Chemical Kinetics and Dynamics*. Prentice-Hall, 1999.

[37] S. Arrhenius. Über die Dissociationswärme und den Einfluss der Temperatur auf den Dissociationsgrad der Elektrolyte. *Zeitschrift für Physikalische Chemie*, 4U(1):96-116, 1889.

[38] U. Burghaus. Review: Surface chemistry of CO2 - Adsorption of carbon dioxide on clean surfaces at ultrahigh vacuum. *Progress of surface science*, 89(2):161-217, 2014.

[39] ADF BAND Documentation. `https://www.scm.com/doc/BAND/index.html`. Accessed: 2018-12-16.

[40] SCM. *Basis sets for ADF and BAND*. 2010.

[41] A. D. Becke. A multicenter numerical integration scheme for polyatomic molecules. *The Journal of Chemical Physics*, 88(4):2547, 1988.

[42] SCM. *Analysis programs*. 2009.

[43] R. S. Mulliken. Electronic Population Analysis on LCAO-MO Molecular Wave Functions. I. *The Journal of Chemical Physics*, 23(10):1833, 1955.

[44] R. F. W. Bader. *Atoms in Molecules; a Quantum mechanical theory*. Oxford University Press, 1994.

[45] J. I. Rodriguez et al. An Efficient Grid-Based Scheme to Compute QTAIM Atomic Properties without Explicit Calculation of Zero-Flux Surfaces. *Journal of Computational Chemistry 30*, 30(7):1082-1092, 2009.

[46] Y. R. Luo. *Comprehensive Handbook of Chemical Bond Energies.* CRC Press, 2007.

[47] R. Davis et al. The orientation of formate and carbonate on ZnO($10\bar{1}0$). *Surface Science Letters*, 298(1):L196-L202, 1993.

[48] G. Pacchioni. Physisorbed and chemisorbed CO2 at surface and step sites of the MgO(100) surface. *Surface science*, 281(1-2):207-219, 1993.

[49] C. Liu, T. R. Cundari and A. K. Wilson. CO2 Reduction on Transition Metal (Fe, Co, Ni, and Cu) Surfaces: In Comparison with Homogeneous Catalysis. *J. Phys. Chem. C*, 2012, 116(9):5681-5688, 2012.

[50] X. Ding et al. Interaction of carbon dioxide with Ni(110): A combined experimental and theoretical study. *Physical Review B*, 76(19):195425, 2007.

[51] I. N. Remediakis, F. Abild-Pedersen and J. K. Nørskov. DFT Study of Formaldehyde and Methanol Synthesis from CO and H2 on Ni(111). *J. Phys. Chem. B*, 108(38):14535-14540, 2004.

NTNU
Norwegian University of
Science and Technology